The Great Deceiver: miR-2392's Hidden Role in Driving SARS-CoV-2 Infection

J. Tyson McDonald[1,2], Francisco Javier Enguita[1,3], Deanne Taylor[1,4,5], Richard A. Bowen[6], Robert J. Griffin[1,7], Waldemar Priebe[1,8], Mark R. Emmett[1,9], Marisa McGrath[10], Mohammad M. Sajadi[10], Anthony D. Harris[11], Jean Clement[10], Joseph M. Dybas[1,4], Nukhet Aykin-Burns[12], Joseph W. Guarnieri[1,13], Larry N. Singh[1,13], Peter Grabham[1,14], Stephen B. Baylin[1,15], Aliza Yousey[1,16], Andrea N. Pearson[16], Peter M. Corry[1,7], Amanda Saravia-Butler[1,17,18], Thomas R. Aunins[19], Prashant Nagpal[19,20,21,22], Cem Meydan[23,24], Jonathan Foox[22,24], Christopher Mozsary[22,24], Bianca Cerqueira[1,25,26], Viktorija Zaksas[1,27], Urminder Singh[1,28], Eve Syrkin Wurtele[1,28], Sylvain V. Costes[18], Diego Galeano[1,29,30], Alberto Paccanaro[1,29,31], Suzanne L. Meinig[32], Robert S. Hagan[32,33], Natalie M Bowman[34], UNC COVID-19 Pathobiology Consortium[35,36+], Matthew C. Wolfgang[32,36], Selin Altinok[37], Nicolae Sapoval[1,38], Todd J. Treangen[1,38], Matthew Frieman[1,10], Charles Vanderburg[39], Douglas C. Wallace[1,13], Jonathan Schisler[1,37], Christopher E. Mason[1,23,24,40,41], Anushree Chatterjee[1,20,21], Robert Meller[1,16], Afshin Beheshti[1,39,42,43,44*]

[1]COVID-19 International Research Team
[2]Department of Radiation Medicine, Georgetown University School of Medicine, Washington D.C. 20007, USA
[3]Instituto de Medicina Molecular João Lobo Antunes, Faculdade de Medicina, Universidade de Lisboa, Av. Prof. Egas Moniz, 1649-028 Lisbon, Portugal
[4]Department of Biomedical and Health Informatics, The Children's Hospital of Philadelphia, Philadelphia, PA 19104 USA
[5]Department of Pediatrics, Perelman School of Medicine, University of Pennsylvania, Philadelphia, PA 19104 USA
[6]Department of Biomedical Sciences, Colorado State University, Fort Collins, CO, USA.
[7]Radiation Biology Division, Dept of Radiation Oncology, University of Arkansas for Medical Sciences, Little Rock, AK, 72211 USA
[8]Department of Experimental Therapeutics, University of Texas MD Anderson Cancer Center, Houston, TX, 77030, USA
[9]Department of Biochemistry and Molecular Biology, University of Texas Medical Branch, Galveston, TX 77555, USA
[10]Institute of Human Virology, University of Maryland School of Medicine, Baltimore, MD, 21201, USA
[11]Department of Epidemiology and Public Health, University of Maryland School of Medicine, Baltimore, MD, 21201, USA
[12]Division of Radiation Health, Department of Pharmaceutical Sciences, University of Arkansas for Medical Sciences, Little Rock, AK, 72211 USA
[13]Center for Mitochondrial and Epigenomic Medicine, Children's Hospital of Philadelphia, Philadelphia, PA 19104, USA
[14]Center for Radiological Research, Columbia University, New York, NY 10032, USA
[15]Department of Oncology, Sidney Kimmel Comprehensive Cancer Center, Johns Hopkins School of Medicine, Baltimore, MD 21287, USA

[16]Department of Neurobiology and Pharmacology, Morehouse School of Medicine, Atlanta, GA 30310, USA
[17]Logyx, LLC, Mountain View, CA 94043, USA
[18]Space Biosciences Division, NASA Ames Research Center, Moffett Field, CA 94035, USA
[19]Department of Chemical and Biological Engineering, University of Colorado Boulder, Boulder, CO, 80303, USA
[20]Sachi Bioworks Inc, Boulder, CO, 80301, USA
[21]Antimicrobial Regeneration Consortium, Boulder, CO, 80301, USA
[22]Quantum Biology Inc, Boulder, CO, 80301, USA
[23]Department of Physiology, Biophysics and Systems Biology, Weill Cornell Medicine, NY, 10065, USA
[24]The HRH Prince Alwaleed Bin Talal Bin Abdulaziz Alsaud Institute for Computational Biomedicine, Weill Cornell Medicine, NY, 10065, USA
[25]KBR Space & Science, San Antonio, TX, 78235, USA
[26]Aeromedical Neurology & Neuroimaging Research Group, United States Air Force School of Aerospace Medicine, Lackland AFB, TX, 78236, USA
[27]Center for Translational Data Science, University of Chicago, Chicago, IL, 60615, USA
[28]Bioinformatics and Computational Biology Program, Center for Metabolic Biology, Department of Genetics, Development and Cell Biology, Iowa State University, Ames, IA 50011, USA
[29]School of Applied Mathematics, Fundação Getulio Vargas, Rio de Janeiro, Brazil
[30]Faculty of Engineering, National University of Asuncion, Central, Paraguay
[31]Department of Computer Science, Centre for Systems and Synthetic Biology, Royal Holloway, University of London, Egham Hill, Egham, UK
[32]Marsico Lung Institute, University of North Carolina at Chapel Hill, Chapel Hill, NC, 27599, USA
[33]Division of Pulmonary Diseases and Critical Care Medicine, Department of Medicine, University of North Carolina, Chapel Hill, NC 27599, USA
[34]Division of Infectious Disease, School of Medicine, University of North Carolina, Chapel Hill, NC, 27599, USA
[35]Department of Oral and Craniofacial Health Sciences, UNC Adams School of Dentistry, University of North Carolina School of Medicine, Chapel Hill, NC, 27599, USA
[36]Department of Microbiology & Immunology, University of North Carolina School of Medicine, Chapel Hill, NC, 27599, USA
[37]McAllister Heart Institute, Department of Pharmacology, and Department of Pathology and Lab Medicine, The University of North Carolina at Chapel Hill, NC 27599, USA
[38]Department of Computer Science, Rice University, Houston, TX 77005, USA
[39]Stanley Center for Psychiatric Research, Broad Institute of MIT and Harvard, Cambridge, MA, 02142, USA
[40]New York Genome Center, NY, USA
[41]The Feil Family Brain and Mind Research Institute, Weill Cornell Medicine, NY, 10065, USA
[42]KBR, Space Biosciences Division, NASA Ames Research Center, Moffett Field, CA, 94035, USA
[43]Senior author

[44]Lead Contact
+The full list of authors associated with the UNC COVID-19 Pathobiology Consortium is available in the supplemental information.
*Correspondence: afshin.beheshti@nasa.gov

Summary (150 words)
MicroRNAs (miRNAs) are small non-coding RNAs involved in post-transcriptional gene regulation that have a major impact on many diseases and provides an exciting avenue towards antiviral therapeutics. From patient transcriptomic data, we have discovered a circulating miRNA, miR-2392, that is directly involved with SARS-CoV-2 machinery during host infection. Specifically, we found that miR-2392 was key in driving downstream suppression of mitochondrial gene expression, increasing inflammation, glycolysis, and hypoxia as well as promoting many symptoms associated with COVID-19 infection. We demonstrate miR-2392 is present in the blood and urine of COVID-19 patients tested, but not detected in COVID-19 negative patients. These findings indicate the potential for developing a novel, minimally invasive, COVID-19 detection method. Lastly, using both *in vitro* human and *in vivo* hamster models, we have developed a novel miRNA-based antiviral therapeutic targeting miR-2392 that significantly reduces SARS-CoV-2 viability and may potentially inhibit a COVID-19 disease state in the host.

Key words
COVID-19, SARS-CoV-2, microRNA, miRNA, Facile Accelerated Specific Therapeutic (FAST), FASTmer, miR-2392, antiviral therapeutic

Introduction

In Fall of 2019, the zoonotic spillover event led to the first know human infection with the severe acute respiratory syndrome coronavirus 2 (SARS-CoV-2) and subsequent human-to-human transmission triggered a pandemic leading to a worldwide health crisis from the resulting disease, referred to as coronavirus disease 2019 (COVID-19) (Huang et al., 2020; Zhu et al., 2020). COVID-19 causes substantial pulmonary disease but can also cause systemic health risks from extrapulmonary manifestations. Its effects entangle the entire body including but not limited to the cardiovascular, gastrointestinal, and hematological systems that may lead to long lasting effects after the virus has left the body, known as PASC (post-acute sequela of COVID-19) (Carfi et al., 2020; Feng et al., 2020; Gupta et al., 2020; Jacobs et al., 2020). SARS-CoV-2 is classified as a member of the Coronaviridae family, a group of viruses with a enveloped positive-stranded RNA that has the ability to infect cross-species (V'Kovski et al., 2021). Currently, three novel vaccines have completed efficacy trials and have been approved for emergency use by the Food and Drug Administration (Baden et al., 2021; Polack et al., 2020; Sadoff et al., 2021). While these vaccines represent a favorable milestone, additional data is required to demonstrate the long-term effectiveness against SARS-CoV-2 and protection against new strains. To prevent an endemic, the complete global eradication of COVID-19 will require a wide majority of the world's population to be vaccinated to achieve herd immunity. Unfortunately, there will always be a portion of the population that will not get vaccinated. Therefore, additional strategies for

antiviral therapeutic options against COVID-19 are particularly relevant and important to explore in order to treat severe illnesses and overcome this global pandemic. Currently the majority of antivirals are repurposed drugs utilized for other disease and have shown limited clinical efficacy, such as remdesivir (Abdelrahman et al., 2021). This brings a needed urgency to develop antivirals specifically designed against SARS-CoV-2.

One potential avenue for an alternative antiviral agent is treatment against specific microRNAs (miRNAs) associated with SARS-CoV-2 infection and subsequent manifestation of COVID-19. MicroRNAs (miRNAs) are non-coding RNAs that are involved with regulation of post-transcriptional gene expression and can impact entire pathways related to viruses and diseases (Jiang et al., 2009; Trobaugh and Klimstra, 2017). Each miRNA can target multiple messenger RNAs (mRNAs) and taken together, miRNAs are predicted to regulate over half of the human transcriptome (Friedman et al., 2009). Recent evidence has shown different diseases, including COVID-19, leads to distinct complements of miRNAs in the blood (Mishra et al., 2020; Nersisyan et al., 2020; Portincasa et al., 2020; Sacar Demirci and Adan, 2020; Sardar et al., 2020; Teodori et al., 2020; Widiasta et al., 2020; Zhang et al., 2021). These circulating miRNAs are highly stable and have the potential to be used for minimally invasive novel detection, potential biomarkers, and therapeutic targets (Tribolet et al., 2020). Research on the interactions between miRNAs and viruses have revealed a multifaceted relationship. Specifically, viruses have been shown to avoid the immune response by leveraging cellular miRNAs to complete their replication cycle (Trobaugh and Klimstra, 2017). The following mechanisms are central to the interaction of viruses and miRNAs: 1) miRNA processing pathways can be blocked or inhibited by viruses interacting with key proteins such as Dicer and associated proteins, 2) viruses can sequester miRNAs resulting in dysregulation of specific target mRNAs, 3) viruses can utilize miRNAs to redirect regulatory pathways of other miRNA targets to provide survival advantages, and 4) viruses can directly encode miRNA precursors that are processed by the canonical miRNA cellular pathway and have well-defined functions to specifically target and regulate the viral replicative cycle (Schult et al., 2018; Trobaugh and Klimstra, 2017).

Here, we report on a miRNA, miR-2392, that may directly regulate and drive a COVID-19 response. This miRNA was initially predicted from COVID-19 patient data that consisted of multiple miRNAs being suppressed/inhibited (miR-10, miR-10a-5p, miR-1-3p, miR-34a-5, miR-30c-5p, miR-29b-3p, miR-155-5p, and miR-124-3p) and one miRNA being upregulated (miR-2392). With further examination, we discovered miR-2392 to be a key miRNA involved with COVID-19 progression. Specifically, miR-2392 drives downstream suppression of mitochondria activity while increasing inflammation, glycolysis, and hypoxia. MiR-2392 upregulation was concomitant with symptoms associated with COVID-19 infection in the host. We found that miR-2392 was circulating in COVID-19 infected patients and increased as a function of viral load. Our results demonstrate that miR-2392 may be utilized as an effective biomarker of COVID-19. Furthermore, we have developed a miR-2392 inhibitor and provide evidence that its use reduces SARS-COV-2 viability in targeted viral screens with A549 cells and reduces the impact of infection in COVID-19 animal models. With further development this miR-2392 inhibitor may represent an effective antiviral therapeutic towards inhibiting the virus and limiting a negative host response from COVID-19.

Results

Identification of key miRNAs associated with COVID-19 infection

Currently, the majority of the published literature associated with miRNAs and SARS-CoV-2 is based on *in silico* predictions. To identify miRNAs that may be involved in driving COVID-19 severity in the host, we first examined publicly available Bronchial Alveolar Lavage Fluid (BALF) RNA-sequencing (RNA-seq) data from 13 individuals. Differential gene expression was assessed using a 1.2-fold change in gene expression for p-values less than 0.01 revealing 42 increased genes and 347 decreased genes, compared to controls. Using the upstream regulator analysis from the Ingenuity Pathway Analysis (IPA) knowledge database, the miRNAs from differentially expressed genes (FDR < 0.05) from COVID-19-positive patients were inferred. Eight miRNAs were predicted to drive significant changes in COVID-19 positive patients with the downregulation of seven miRNAs (miR-10, miR-1, miR-34a-5p, miR-30c-5p, miR-29b-3p, miR-124-3p, and miR-155-5p) and upregulation of a single miRNA, miR-2392 (**Fig. 1A**). Using IPA's downstream effects analysis to predict biological processes from the combined suppression of the seven miRNAs and the upregulation of miR-2392 resulted in increased inflammation, immune suppression, and suppression of mitochondrial activity in the BALF dataset (**Fig. 1B and 1C**).

In support of these findings, previous studies have shown alterations in specific miRNAs may directly impact viral infections. For example, upregulation of miR-10, miR-124, or miR-1 have been shown to have antiviral roles during infection (Hu et al., 2020; Sardar et al., 2020; Yang et al., 2016). Interestingly, upregulation of miR-30 and miR-155 have been shown independently to provide suppression in other types of coronaviruses (Dickey et al., 2016; Ma et al., 2018). The one miRNA predicted to be upregulated in COVID-19 patients from the BALF data was miR-2392. Though limited, the existing literature on miR-2392 demonstrates it is related to mitochondrial suppression and increased glycolysis (Fan et al., 2019) and circulating factors related to negative health risks (Chen et al., 2013; Fan et al., 2019; Hou et al., 2019; Li et al., 2017; Park et al., 2014; Yang et al., 2019).

Pathway analysis was performed with targets and pathways for miR-2392 to determine its impact on the host when upregulated. We observed that the upregulation of miR-2392 in the RNA-seq dataset impacted many downstream targets and pathways related to negative health outcomes (**Fig. 1C**). In addition to mitochondrial suppression, we also predicted activation of factors related to reactive oxygen species (ROS). Alternatively, since it is known that miR-2392 directly interacts with the mitochondrial DNA (mtDNA) to inhibit the levels of many of the mtDNA coded oxidative phosphorylation transcripts, this could be a compensatory response to the inhibition of mitochondrial bioenergetics.

Glycolytic pathways (**Fig. 1C**) are also upregulated in association with increased miR-2392. MiR-2392 drives both hexokinase 2 (HK2) and pyruvate kinase (PKM) which are both positive regulators of glycolysis. HK2 phosphorylates glucose to produce glucose-6-phosphate and is a primary regulator of glycolysis. HK2 further enhances GDP-glucose biosynthesis. GDP-glucose is a nucleotide sugar which an essential substrate for all glycosylation reactions (i.e. glycosylation of viral spike proteins). Pyruvate kinase is essential for the production of ATP in

glycolysis as this enzyme catalyzes the transfer of the phosphate group from phosphoenolpyruvate to ADP to make ATP. The mechanism of how miR-2392 is driving these pathways is not clearly understood, but one possibility could be due to the stabilization of glycolytic transcripts.

Overall, the miR-2392 observed upregulation of glycolysis and antiviral effects related to miR-2392 suppression are consistent with the recently documented role of glucose metabolism in the progression of viral infection and poor outcome of COVID-19 (Ardestani and Azizi, 2021). It is also consistent with the reported effects of suppression of glycolysis by inhibitors like the glucose analog, 2-deoxy-D-glucose (2-DG), that was shown to suppress SARS-CoV-2 replication in *in vitro* models (Ardestani and Azizi, 2021; Bojkova et al., 2020; Codo et al., 2020). Interestingly, 2-DG is also 2-deoxy-D-mannose and as such can interfere with processes utilizing mannose, a monosaccharide that is *in vivo* produced from glucose. Mannose plays important roles in the glycosylation of specific proteins. Replacement of a mannose molecule by 2-DG in the respective SARS-CoV-2 N-glycans or O-glycans might lead to their truncation and subsequently to the suppression of virus infectivity and proliferation. These and miR-2392 data clearly indicate that selective targeting of glucose metabolism might have significant impact on current and future SARS-CoV-2 pandemics.

Targets related to the goals of antioxidant N-acetyl cysteine (NAC) therapy are also observed to be upregulated. These include activated endothelial cell increasing their expression of numerous adhesion molecules, including intercellular adhesion molecule 1 (ICAM1), vascular cell adhesion molecule 1 (VCAM1), and E-selectin, which allow attachment of hematopoietic immune and non-immune cells to the endothelial surface, and thus, contribute to inflammation and activation of the coagulation cascade. Powerful antioxidants such as NAC counteract COVID19 infections by potentially suppressing viral replication via improving intracellular thiol redox ratio as a precursor for major thiol antioxidant glutathione (Ho and Douglas, 1992) and inhibiting the NF-kB pathway (Poppe et al., 2017). Inhibition of the NF-κB pathway has been shown to reduce inflammatory damage by altering the glutathione and glutathione disulfide ratio (Aykin-Burns et al., 2005; Griffin et al., 2003; Jia et al., 2010). Because NAC can also modulate oxidative burst and reduce cytokine storm without weakening the phagocytizing function of neutrophils (Allegra et al., 2002; Kharazmi et al., 1988; Sadowska et al., 2006), its use in COVID-19 patients as a single agent or in combination with other antioxidants are being conducted in clinical trials (Alamdari et al., 2020). A recent study has shown noteworthy benefits of NAC in patients with severe COVID-19 infection (Ibrahim et al., 2020). Major mechanisms proposed for these favorable patient outcomes were NAC's ability to reduce IL-6 induced mitochondrial oxidative stress via Complex I inhibition as well as to prevent increased inflammation due to uncontrolled activation of mTORC1. These results were in line with the role of miR-2392 in reducing the activities of electron transport chain complexes and enhancing glycolysis, which is known to be induced by mTORC1 activation. The same study also speculated that NAC could inhibit SARS-CoV-2 binding to ACE2 by reducing disulfide bonds in its receptor-binding domain. Inflammatory pathways and others that are observed with COVID-19 infection were also seen to be activated downstream of miR-2392.

Conservation of miR-2392 between species and its predicted interactions with the SARS-CoV-2 genome

Viral miRNAs can play a role in interspecies transmission due to the high conservation of miRNAs among species and the ability of viruses to integrate miRNAs into its own genome (Sacar Demirci and Adan, 2020; Schult et al., 2018). In addition, such integration of miRNAs within the virus has been shown to assist viruses to replicate and evade the immune system (Islam and Islam, 2021). To determine if miR-2392 might be capable of driving the observed COVID-19 health risks and symptoms in the host, we analyzed the conservation of human miR-2392 across species and the integration of miR-2392 into the SARS-CoV-2 genome (**Fig. 2**).

The UCSC Genome Browser was utilized to determine the conservation of miR-2392 across different species (Kent et al., 2002). The mature 20 base-pair miR-2392 is derived from an 84 base-pair region of the 3´-UTR in the long non-coding RNA (lncRNA) gene, maternally expressed 3 (MEG3) and located in an imprinted region DLK1-DIO3 that also contains three clusters for the expression of 51 additional miRNAs (**Fig. 2A and 2B**). A base wise evolutionary conservation comparison demonstrated that miR-2392 is highly conserved among non-human primates. In addition, conservation of miR-2392 is evident in dogs, cats, and ferrets, species known to be infected with SARS-CoV-2 while mice and rats, species not impacted by COVID-19 (Johansen et al., 2020), have poor conservation with miR-2392.

To determine the impact of miR-2392 on normal tissues, we studied the impact of miR-2392's host gene, MEG3, on normal tissues utilizing GTEx data (Consortium, 2020). For the majority of healthy tissues, MEG3 was either not detected or being expressed at low levels (**Fig. 2B**). This can imply that miR-2392 does not seem to significantly affect normal tissues.

To explore potential binding sites for miR-2392, we used the miRanda software (Enright et al., 2003) to identify all potential binding sites with respect to the SARS-CoV-2 reference genome (Wuhan-Hu-1; NC045512.2) and representative genomes from lineages of concern. We found that the miR-2392 seeding region is heavily integrated within SARS-CoV-2 and conserved in different viral strains (**Fig. 2C**). The three best hits from the miRanda scores are located in the NSP2, NSP3, and E-genes. Notably, these regions were conserved among 6 variants and lineages of concern each represented by 14 recent genomes from the respective lineage available from the Global Initiative on Sharing All Influenza Data (GISAID, (Shu and McCauley, 2017)).

MiR-2392 targets mitochondrial and inflammatory pathways associated with SARS-CoV-2

To determine in more detail the specific impact of miR-2392 gene targets and pathways in COVID-19 patients, miR-2392 gene targets were retrieved from the miRmap database as predicted by base pairing with its seed-region (Vejnar and Zdobnov, 2012). This list was further refined by overlap found in several other miRNA databases including miRmap (Vejnar and Zdobnov, 2012), miRwalk (Dweep and Gretz, 2015), miRDB (Chen and Wang, 2020), miRnet (Chang et al., 2020b), and ClueGo (Bindea et al., 2009). We also included RNA-seq analysis of 39 autopsy tissue samples from the heart, lung, kidney, liver, and lymph node of COVID-19-positive patients with high or low viral loads (Park et al., 2021). The refined list of miR-2392 gene targets (consisting of 375 genes) was examined using volcano plots in all samples (**Fig. 3A-F**).

To better determine the systemic impact on miR-2392 gene targets in COVID-19, we performed pathway analysis from the nasopharyngeal swab samples in living donors with and without COVID-19 using the SARS-CoV-2 viral load as the independent variable (high, medium, low, other virus). The miR-2392 gene targets are differentially expressed (FDR<0.05) in at least one comparison of COVID-19-positive patients or other detected virus and were found to separate into six distinct hierarchical clusters that were identified and annotated utilizing ShinyGO (Ge et al., 2020) to determine the major pathways altered (**Fig. 3G**). The majority of these upregulated miR-2392 targets are involved in immune and inflammatory pathways. The downregulated miR-2392 targets were involved in mitochondrial function, oxidative stress, cell cycle, developmental biology, and ubiquitin binding which are pathways recently associated with the SARS-CoV-2 infection process (Hemmat et al., 2021). This data demonstrates miR-2392 may target several gene pathways related to perpetuating SARS-CoV-2 infection. For the majority of the tissues (excluding the lymph nodes), higher viral loads are associated with greater miR-2392 gene targets being regulated. Interestingly, the lymph nodes show an inverse relationship with viral loads compared to other tissues.

Because miR-2392 was recently shown to directly target the transcription of mitochondrial DNA genes (Fan et al., 2019), we evaluated the impact on expression of the mitochondrial miR-2392 targets in our datasets. Differentially expressed miR-2392 target mitochondrial genes were identified using the MitoCarta database (Rath et al., 2021) (**Fig. 3H**). This revealed 14 genes harboring miR-2392 seed sequences that were significantly dysregulated in the nasal and heart samples. In nasal samples, SLC25A28, mitoferrin which mediates mitochondrial iron transport, was strongly upregulated along with IBA57, which is involved in iron sulfur assembly. The mitochondrial outer membrane protein import complex subunit TOMM20, cytochrome c oxidase (complex IV) subunit COX6B1, and mitochondrial transcription factor COT-2 (NR2F2) were strongly down regulated. In the heart, the folate enzyme MTHFD2L (methylenetetrahydrofolate dehydrogenase) was up-regulated while all of the other nuclear-coded mitochondrial genes identified were down regulated. Downregulated heart mitochondrial genes included NDUFS5 (complex I subunit), COX6B1 and COX10 (complex IV structural and assembly subunits), CKMT1A (mitochondrial creatine kinase), MRPL34 (subunit of the large subunit of the mitochondrial ribosome), COT-2 (NR2F2), AK4 and MSRB3 (adenylate kinase 4 and methionine-R-sulfoxide reductase which mitigate oxidative stress), MRS2 (magnesium transporter) and CLIC4 (chloride channel). The kidney showed mild upregulation of complex I and single methyl group metabolism, but down regulation of complex IV (COX10), regulatory factor (COT-2), and iron sulfur center protein (IBA57). Hence, SARS-CoV-2 seems to downregulate nuclear mitochondrial gene transcription in the more oxidative heart and kidney, as well as in nasal tissues.

Since inflammation is a key component of COVID-19 infection, we also overlaid the standard known inflammatory genes determined from Loza et al. (Loza et al., 2007) to the miR-2392 targets (**Fig. 3I**). The analysis reveals that, at the mRNA level, most of the complement pathway genes are upregulated in the tissue samples analyzed. These changes could be compensatory, as proteins encoded by the genes could be downregulated as a function of traditional miRNA effects. The responses reflect the importance of degrees of inflammation for

mediation of disease severity in COVID-19 patients and a key modulatory role of miR-2392 in this context.

Proteomic and transcriptomic analysis on miR-2392 targets on blood from COVID patients utilizing COVIDome (Sullivan et al., 2021) revealed interesting patterns between RNA and protein levels for miR-2392 targets (**Fig. 3J and 3K**). We utilized the miR-2392 gene targets only determined through miRmap to determine a broader relationship between the proteins and genes. Several miR-2392 targets in the tissue show a significant transcription increase in COVID-19-positive samples with small to no changes on the proteomics level: PLK1, CD38, PYCR1, RNASE1, BIRC5, RRM2, SIGLEC1 (**Fig. 3J**). Interestingly, all these genes were also positively regulated for the majority of tissues when considering only miR-2392 gene targets with miRmap (**Figs. S1 and S2**). In the blood, the miR-2392 targets CXCL10, STAT1, IFIT3, and C1QC were positively regulated at both the protein and gene levels. This upregulation was also observed in all other tissues (**Figs. S1 and S2**). We explored the correlation between RNA expression and protein abundance for miR-2392 targets in COVID-19 positive and negative samples (**Fig. 3K**). Pearson correlation in both sample types is very close, with a slightly stronger value in COVID-19 negative samples (negative samples cor=0.2089863, p-value=4e-10, positive samples cor=0.2053345, p-value=8e-10). Further investigation is needed to understand if increased levels of miR-2392 could potentially bind genes' mRNAs at a higher rate and therefore prevent translation to protein or if there are other mechanisms preventing mRNA translation to protein.

Overexpression of miR-2392 simulates a phenotype similar to COVID-19 infection

To determine if the upregulation of miR-2392 alone would elicit effects similar to a COVID-19 infection, cells were treated with a miR-2392 mimic. Using RNA-seq data, there were 649 genes with a fold-change greater than ±1.2 and a p-value less than 0.05 (**Fig. 4A**). A number of these differentially expressed genes were predicted targets of miR-2392 (**Fig. 4B**). Of particular interest are differentially expressed genes in this model that are also dysregulated in SARS-CoV-2 infected cells. We analyzed whole cell proteome data from a human-derived cell culture model for a SARS-CoV-2 infection profile (Stukalov et al., 2021), and found 10 proteins that were significantly changed in abundance and were also altered with miR-2392 overexpression: KIF22, FKBP14, RAD51, AFAP1, ZCCHC17, ZWINT, MAGED1, CENPF, TMEM70, and NFKB2 (**Fig. 4C**). Viral infection is associated with alterations in protein posttranslational modifications of cellular proteins, including ubiquitination. This phenomenon can occur by viral or host directed modifications. We analyzed the ubiquitinome of the human-derived cell culture model of SARS-CoV-2 infection and observed a number of proteins that were increased or decreased in normalized ubiquitin abundance and were also dysregulated genes by miR-2392 overexpression. Furthermore, we found miR-2392 overexpression impacted genes involved with mitochondria, and inflammation (**Fig. 4D-4F**).

To determine if there was a direct correlation between miR-2392 overexpression and SARS-CoV-2 infection, comparisons were made using gene expression fold-change values or overlap in statically significant curated gene sets from canonical pathways determined by our fGSEA analysis. Using previously published data from Blanco-Melo *et al.* (Blanco-Melo et al., 2020), showed there was a statistically significant and positive correlation of the miR-2392 treatment

compared to both the A549 and Calu-3 cell culture models infected with SARS-CoV-2 (**Fig. 4G and 4H**) as well as in lung biopsies post-mortem from two COVID-19 positive patients (**Fig. 4H**). Using nasal swab samples, a significant and positive correlation was determined between patients with medium- and low-viral loads compared to non-infected patients (**Fig. 4I and 4J**). Further identification of miR-2392 correlation to SARS-CoV-2 infections was made using RNA-seq from multiple tissues (heart, kidney, liver, lymph node, and lung) obtained during autopsies of COVID-19 patients with high or low viral loads (**Fig. 4I-J**). There was a positive correlation to lung and lymph node tissues with miR-2392 expression. Interestingly, there was a significant and positive correlation to liver tissue when comparing gene fold-change values (**Fig. 4I**) but not fGSEA curated biological genesets (**Fig. 4J**). In contrast, a negative correlation to heart tissue was observed.

Statistically significant pathways that were enriched due to miR-2392 treatment were examined using fGSEA **(Fig. 4K-O)**. It was observed that the miR-2392 treatment induced pathway response that was significantly related to SARS-CoV-2 pathways. One obvious relationship shows that the Reactome SARS-CoV-2 pathways were significantly activated for the miR-2392 treated cells compared to the controls (**Fig. 4K and 4L**). Significant Hallmark pathways (**Fig. 4N**) show distinct pathways that have been reported to be associated with COVID-19 in patients, such as upregulation of hypoxia (Herrmann et al., 2020), glycolysis (Ardestani and Azizi, 2021), and cell cycle pathways (Su et al., 2020). Interestingly, the KEGG pathway analysis (**Fig. 4M**) indicates the overexpression of miR-2392 treated highly upregulated systemic lupus erythematosus which has been reported to occur in COVID-19 patients and have shown similar pathologies due to the increase of inflammation (Zamani et al., 2021).

Lastly, we determined the impact of miR-2392 specific targets being downregulated in the cell lines after miR-2392 overexpression. A regulatory network was built by including the predicted miR-2392 targets in the microRNA Data Integration Portal (MIRDIP) that were also downregulated in the overexpression cell model as well as from the recently described consensus transcriptional regulatory networks in coronavirus infected cells (Ochsner et al., 2020) (**Fig. 4P**). The gene enrichment analysis of these putative miR-2392 targets showed the presence of GO-terms related with the RNA metabolism, transcription, ribosome activity and Golgi complex (**Fig. 4Q**).

Circulating miR-2392 and the suppression of other miRNAs in COVID-19 infected patients

To demonstrate the presence of circulating miR-2392 in COVID-19 infected patients, we quantified the amount of miR-2392 by droplet digital PCR (ddPCR) in the serum, urine and nasopharyngeal swab samples (**Fig. 5**). For the serum there were ten COVID-19 positive intubated patients, ten COVID-19 positive patients (not intubated), and ten negative patients. For the urine samples there were 15 inpatient COVID-19 positive samples, 15 outpatient COVID-19 positive samples, 10 inpatient COVID-19 negative samples, and 11 COVID-19 negative healthy donors. Lastly, we quantified nasopharyngeal swab samples from 10 COVID-19 positive patient samples, 6 common cold coronavirus positive patient samples (229E, HKU1, and OC43), and 6 Respiratory Illness/Coronavirus NL63 positive patient samples. In addition, we also quantified three other miRNAs which we predicted to be inhibited by COVID-19 infection (**Fig. 1A**) which were: miR-1-3p (**Fig. S3**), miR-155-5p (**Fig. S4**), and miR-124-3p (**Fig. S5**).

We observed a statistically significant increase of miR-2392 in COVID-19 positive patients from both the serum and urine samples (**Fig. 5A**). In addition, Receiver Operating Characteristic (ROC) curve analysis revealed that miR-2392 is significantly associated with SARS-CoV-2 infection in patients (**Fig. 5B**) in all tissues. Lastly, when dissecting the amounts of miR-2392 with specific conditions associated with infection, we observe that more severely affected patients (i.e. intubated patients or patients in ICU), had higher presence of miR-2392 (**Fig. 5C**). Interestingly, low levels miR-2392 appeared in the nasopharyngeal location with no significant differences occurring between seasonal coronavirus samples. Since we hypothesize that miR-2392 is a primary initiator for systemic impact of the infection, this might indicate that miR-2392 does not strongly appear until the virus has established its presence in the body.

As mentioned above we also measured the quantity of miR-1-3p (**Fig. S3**), miR-155-5p (**Fig. S4**), and miR-124-3p (**Fig. S5**) and performed the same analysis. For miR-1-3p we observed significant suppression in the serum while no significant differences in the urine or nasopharyngeal samples (**Fig. S3**). MiR-1-3p is known to be beneficial for cardiovascular functions, with the inhibition of miR-1-3p leading to heart failure and heart disease (Condorelli et al., 2010). Similar response was observed for miR-155-5p with significant suppression in the serum while no significant differences in the urine or nasopharyngeal samples (**Fig. S4**). For miR-124-3p, we observed very low amounts (on average < 2 copies/5 ng RNA), for all conditions, which indicates that miR-124-3p is not circulating for any of the patients for any the conditions observed (**Fig. S5**). MiR-124-3p provides as an ideal miRNA negative control candidate for SARS-COV-2.

Inhibiting miR-2392: a novel antiviral COVID-19 therapeutic

The link that we found between miR-2392 and COVID-19 infection prompted us to ask whether we could develop effective antivirals for COVID-19 by inhibiting miR-2392. We used the Facile Accelerated Specific Therapeutic (FAST) platform to develop an effective antisense-based therapeutic against human miR-2392 (Aunins et al., 2020; Eller et al., 2021), termed SBCov207, for the treatment of COVID-19 (**Fig. 6A**). The FAST platform combines the four essential modules of drug development cycle (design, build, test, and learn) to optimize therapeutics against any gene and species of interest in less than a week. The anti-miR-2392 FASTmer was evaluated for efficacy and toxicity against a SARS-CoV-2 infection of the human lung cell line A549 (**Fig. 6B-D**). Treatment of uninfected A549 cells showed no cytotoxicity up to 20 µM. The control nonsense FASTmer (SBCoV208) showed no toxicity even up to 40 µM. Treatment of A549 cells infected with SARS-CoV2 showed drastic improvement in cell viability with an average of 85% viral inhibition at 10 µM (IC50 of 1.15 ± 0.33 µM). In contrast, the control nonsense FASTmer showed significantly lower viral suppression (**Fig. 6E-G**). Human cell line-based infection models reaffirm that the anti-miR-2392 (SBCov207) is effective in inhibiting SARS-CoV2, while not exhibiting toxicity at the concentrations tested.

In a separate *in vivo* model, the anti-miR-2392 FASTmer was evaluated in a Syrian hamster infection model (**Fig. 6H-6J**). Initially six hamsters were treated with FASTmers for 72 hours without infection to observe any changes in animal behavior indicating toxicity. There were no observed changes in animal behavior indicating a lack of obvious toxicity. Following this study, 30 male hamsters were divided into 5 treatment groups. The infected hamsters were given 10^5

plaque forming units (pfu) of WA01/2020 strain of SARS-CoV-2 passaged twice in Vero E6 cells from the original isolate obtained from BEI Resources. The anti-miR-2392 FASTmer treatment was given by intraperitoneal (IP) injection or intranasal (IN) instillation 24 hours before viral inoculation or both 24 hours before and 24 hours after viral inoculation. Each FASTmer dose was at a concentration of 10 µM in a 100 µL volume (approximately 0.13 mg/kg). Half of the hamsters in each group (n = 3) were euthanized and necropsied on day 3 and 7 post-infection respectively.

Loss of body weight of hamsters over the course of the experiment were <10% in all groups and significantly different for the IN treatment one day before viral inoculation (compared to the control) and while statistical differences between other groups were not present (**Fig. 6H**). Virus titers from oropharyngeal swabs of hamsters receiving IN treatment were significantly lower (p = 0.018) than those from hamsters receiving FASTmers IP or PBS on day 1 post-challenge, but there were no differences among groups in magnitude of shedding on days 2 and 3 post-challenge (**Fig. 6I**). Although not statistically different than the control treatment, the data indicates a downward trend with FASTmer treatment (**Fig. 6J**). In addition, the total histopathological score for the IN was lower than the controls although not significant.

The impact of miR-2392 on diseases, relationship to COVID-19 symptoms, and predicted FDA drugs to target miR-2392

To predict whether miR-2392 might have a direct relationship to COVID-19 symptoms in the host, we determined the pathway and disease relevance of miR-2392 using miRnet (Chang et al., 2020b). Among the diseases predicted to be associated with miR-2392 were a surprising number of clinical observations present in individuals with COVID-19 infection (**Fig. 7A**). These include heart or cardiovascular disease and failure, both known to heavily contribute to morbidity and mortality in patients with COVID-19 (Nishiga et al., 2020), hyperesthesia (Krajewski et al., 2021), as well as less common COVID-19 symptoms, such as lymphadenopathy and pharyngitis related to sore throat (Edmonds et al., 2021; Walsh-Messinger et al., 2020), liver dysfunction (Portincasa et al., 2020), splenomegaly (Malik et al., 2020), CNS (Mahajan and Mason, 2021; Rodriguez et al., 2020) and kidney failure (Hultstrom et al., 2021).

It is interesting to note that miR-2392 was also predicted to affect diseases that appeared not to be associated with COVID-19 infection, but literature searches reveal these pathologies do occur in some COVID-19 patients. For example, azoospermia, which is linked to male infertility, has been shown to occur in some male patients (Younis et al., 2020). The menstrual cycle in females have been reported to be deregulated for months after COVID-19 infection (Li et al., 2021). Association with dental damage has also been observed in COVID-19 patients (Sirin and Ozcelik, 2021), also deafness or hearing loss (Koumpa et al., 2020). We used the tool Kaplan-Meier Plotter (Nagy et al., 2018) to associate miR-2392 expression with pan-cancer patient survival (**Fig. S7**). We observed that the high expression of miR-2392 is generally related to poor prognosis with the majority of cancer types (p-value < 0.05). If miR-2392 is associated with COVID-19, as we are hypothesizing, and is persistent after the virus clears the host, then the implications for the potential long-term impact on the millions of people infected with COVID-19 could be devastating. Intriguingly, one of the miR-2392 predicted consequences in the

immune category is decreased antibody levels in the blood; this might account for the reported loss of the antibodies overtime (Gudbjartsson et al., 2020; Self et al., 2020).

Using computational prediction models, we also predicted small molecules, including FDA-approved drugs that could inhibit miR-2392 from two different approaches. The first approach employed a state-of-the-art machine learning method that we recently developed for predicting missing drug targets (Galeano et al., 2021). We applied this algorithm on an association dataset between 213 small molecules and 1,519 miRNAs from the SM2miR database (Liu et al., 2013) (see statistics in **Fig. S8**). Our model also integrated chemical similarity between small molecules and sequence similarity between miRNAs. In ten-fold cross-validation experiments, we achieved an average area under the receiver operating curve of 0.877 when predicting missing small molecule-miRNA associations (**Fig. S9**). A list of the top-20 predicted small molecules for miR-2392 (**Fig. 7B**) includes Dexamethasone, the first drug known to save lives in critically ill COVID-19 patients (Ledford, 2020), and Atorvastatin, that has shown similar protective role in COVID-19 patients (Rossi et al., 2020). The second approach follows ideas first presented in Sirota *et al.* (Sirota et al., 2011)and consists on analyzing the genomic signature of miR-2392 (*i.e.* significant up and down-regulated genes) and predicting small molecules that can reverse it. We screened the genomic signature of miR-2392 against the genomic signature of 30,000 small molecules contained in the connectivity map (CMAP) (Lamb et al., 2006). The top-20 small molecules predicted by our approach (Sirota et al., 2011) includes the androgen receptor antagonist Enzalutamide and the insulin sensitizer Pioglitazone (Carboni et al., 2020) both of which are in clinical trials for COVID-19 (**Fig. 7C;** Clinical Trial #NCT04475601 and NCT04604223). We also found literature evidence for the leukotriene inhibitor ubenimex (Asai et al., 2020), and the bacterial DNA inhibitor metronidazole (Gharebaghi et al., 2020).

Discussion

While the potential eradication of the novel coronavirus through worldwide vaccination is underway, there remains a major need to develop effective interventional strategies to minimize the damage caused by coronavirus infections. Host-mediated lung inflammation is a driver of mortality in COVID-19 critically ill patients. Thus, it is logical to focus on therapeutics that may have immunomodulating properties or disrupt viral replication. Our research uncovers a novel eight miRNA signature in patients with COVID-19 viral loads compared to those without disease as predicted from RNA-seq data. The expression of seven miRNAs was decreased (miR-10, miR-1, miR-34a-5p, miR-30c-5p, miR-29b-3p, miR-124-3p, and miR-155-5p) while a single miRNA, miR-2392, was significantly increased (**Fig. 1**). This key miRNA signature was involved in major cellular and molecular mechanisms that drives the viral-host response.

From previous research, the upregulation of miR-10a-5p, from the miR-10 precursor miRNA, provides antiviral benefits through the suppression of SDC1 that can act as a defense mechanism for Porcine hemagglutinating encephalomyelitis viruses (Hu et al., 2020). The upregulation of miR-124 is shown to inhibit the Japanese encephalitis virus replication (Yang et al., 2016). Notably, the upregulation of mir-30c-5p and miR-155-5p have been independently shown to be involved with antiviral functions through immune and inflammatory pathways with other type of coronaviruses (Dickey et al., 2016; Ma et al., 2018). It was also indicated that inhibition of miR-34a-5p in the host by SARS-CoV-2 suppresses beneficial antiviral pathways

that this miRNA regulates. (Bartoszewski et al., 2020; Sacar Demirci and Adan, 2020). miR-1-3p has previously been identified as an antiviral agent for viral related respiratory diseases and the downregulation by SARS-CoV-2 is predicted to follow similar pathways for survival in the host (Sardar et al., 2020). Examination of patients with COVID-19 showed increased levels of miR-2392 circulating blood (**Fig. 5**). Interestingly, we show that for both miR-1-3p and miR-155-5p from serum patient samples were significantly inhibited (**Figs. S3 and S4**), which is in agreement with the current viral literature as discussed above. MiR-124-3p was shown to have no significant changes and barely present for SARS-CoV-2 patients (**Fig. S5**), indicating the responses discussed above is potentially specific for Japanese encephalitis virus.

Several studies have measured differential expression of miRNAs in COVID-19 patients and proposed their use as biomarkers or therapeutics. A post-mortem examination from lung biopsies in nine COVID-19 patients compared to controls found miR-26a, miR-29b, and miR-34a were correlated to endothelial dysfunction and inflammatory biomarkers (Centa et al., 2020). In a separate study performing multi-transcriptome sequencing in red blood cell depleted whole blood from moderate or server COVID-19 patients four additional miRNAs, miR-146a, miR-21, miR-142, and miR-15b, were identified as potential biomarkers as well as contributors to disease pathogenesis (Tang et al., 2020). It has also been suggested to use miRNAs to target the angiotensin-converting enzyme 2 (ACE2) receptor that facilities endocytosis of viral particles into the cells to limit virus-induced glomerular injury, cell infection, kidney damage (Mishra et al., 2020; Nersisyan et al., 2020; Pontecorvi et al., 2020; Sacar Demirci and Adan, 2020; Sardar et al., 2020; Teodori et al., 2020; Widiasta et al., 2020). While these studies are limited to a specific tissue, our data that correlates miRNA signatures from multiple tissues (**Fig. 3**) suggests miR-2392 is a unique target that is ubiquitously involved in COVID-19 symptoms.

In 2010, miR-2392 was found in a small-RNA deep-sequencing of normal and malignant human B-cells where it was altered among hundreds of other microRNAs (Jima et al., 2010). Since then, the majority of publications with miR-2392 are focused on cancer tissues and have found a potential role for miR-2392 in driving cellular invasion and metastasis through an epithelial-mesenchymal transition. In 2013, miR-2392 was one of 6 circulating microRNAs altered in the serum and tissue of patients with cervical squamous cell carcinoma that was used to predict the occurrence of lymph node metastasis with the potential to assist in clinical staging (Chen et al., 2013). Higher levels of miR-2392 in gastric cancer was found to be associated with lower clinical staging and increased patient survival (Li et al., 2017). It was shown that miR-2392 inhibited gastric cell invasion and metastasis by targeting MAML3 and WHSC1 for degradation that subsequently decreased an epithelial-mesenchymal transition through the loss of Snail1, Slug, and Twist1 expression. Similarly, miR-2392 and miR-1587 were found to target the ZEB2 protein, a promoter of the epithelial-mesenchymal transition. A lower expression of these two miRNAs were found in human keloid tissues that resulted in a loss of inhibition of ZEB2 and subsequent promotion of cellular proliferation and invasion in keloids (Hou et al., 2019). Inhibition of miR-2392 by the long-non-coding RNA CACNA1G-AS1 was found to promote hepatocellular carcinoma through disrupting the degradation of C1orf61, a tumor activator associated with metastasis and tumor progression (Hu et al., 2013; Yang et al., 2019). Recently, Fan et al. demonstrated a novel role for miR-2392 in the regulation of chemoresistance in tongue squamous cell carcinoma by partial inhibition of mitochondrial DNA (mtDNA) transcription

through direct miRNA-mtDNA base pairing which resulted in reprogramming tumor cell metabolism (Fan et al., 2019). These reports for miR-2392 establish the significant impact this single miRNA may have in on cellular activity. Particularly relevant to this study was the altered expression of miR-2392 found in Hepatitis B viral infections. Its expression was found to be increased by more than 2-fold in extracellular vesicles secreted from human hepatocytes infected with the Hepatitis B virus (Enomoto et al., 2017). While miR-2392 has a reported impact on tumor cell biology, our study expands the valuable therapeutic potential of targeting miR-2392 to subsequently decrease SARS-CoV-2 viral infections (**Fig. 6**). These results warrant further exploration of the mechanistic underpinnings for the role of miR-2392 in driving viral infection.

One therapeutic insight deduced from miR-2392 interactions is the importance of the mitochondrial oxidative phosphorylation (OXPHOS) and glycolytic pathways in COVID-19, dramatically highlighted in BALF samples reported in **Fig. 1C**. In a study of tongue squamous cell carcinoma (Fan et al., 2019) it was reported that miR-2392 enters the mitochondrion where it binds to Ago2 and then binds to nucleotides 4379 to 4401 in the mtDNA heavy (H) strand. This binding site is within the MT-TQ (tRNA glutamine) gene, which encompasses nucleotides m.4329-4400. MT-TQ is part of a large polycistronic transcript transcribed from the H-strand promoter. This transcript encompasses 12 of the mtDNA H strand polypeptide genes punctuated by tRNAs. Cleavage of the tRNAs releases the mRNAs. Up-stream of TM-TQ are the 12S and 16S rRNAs and the complex I gene MT-ND1 gene. Downstream of MT-TQ is MT-ND2, MT-CO1, MT-CO2, MT-ATP6/8, MT-ND3, MT-ND4L, MT-ND4, MT-ND5, and MT-CYB (Lott et al., 2013; Wallace, 2018). Strikingly, the down-regulated mtDNA genes from the BALFS are the complex IV (cytochrome c oxidase) genes MT-CO1 and MT-CO2, the complex III (the bc_1 complex) gene (MT-CYB), and the complex I genes (MT-ND2, MT-ND4, and MT-ND5) (**Fig. 1C** right side arc). Since the miR-2392 inhibition of mtDNA OXPHOS genes shown for the BALF samples (**Fig. 1C**) is also reflected in the miR-2392 down-regulation of the nuclear DNA coded mitochondrial transcripts of the complex I and IV genes and the iron-sulfur and heme iron complexes in the nasal, heart, and kidney autopsy samples (**Fig. 3D**), mitochondrial inhibition by miR-2392 appears to be the only physiological function that is common across all tissues in infected individuals. This suggests that mitochondrial modulation is a central feature of SARS-CoV-2 pathophysiology.

The inhibition of mitochondrial genes by miR-2392 would impair OXPHOS, which would have the most adverse effects on the high mitochondrial energetic tissues (brain, heart, kidney), the tissues central to the most severe COVID-19 cases. Inhibition of mitochondrial OXPHOS genes would increase mitochondrial reactive oxygen species (mROS) production, and induce glycolysis to compensate for the energy deficit (see top of **Fig 1C**). Mitochondrial function is regulated by the Sirtuins (Carrico et al., 2018), mitochondrial decline is associated with senescence, and mROS oxidation of mtDNA is linked to activation of the inflammasome and thus NFκB (West et al., 2015; West and Shadel, 2017; Zhong et al., 2018), all of which are modulated around miR-2392 (**Fig. 1C**). Thus, SARS-CoV-2 induction of miR-2392 (**Fig. 5**) and its associated inhibition of mtDNA and nuclear DNA OXPHOS genes (**Fig. 3** and **S1**) could explain many of the metabolic disturbances of COVID-19. Conversely, antagonism of miR-2392 function should ameliorate the inhibition of OXPHOS and may explain the therapeutic benefit of the anti-miR-2392 FASTmers.

Using miRNAs from serum as a biomarker was first established in patients for the examination of diffuse large B-cell lymphoma (Lawrie et al., 2008). The use of miRNAs as a diagnostic biomarker has several advantages. Circulating miRNAs are readily obtained through a minimally invasive blood draw and are remarkably resistant to degradation in the plasma and serum (Mitchell et al., 2008). Measuring differentially expressed miRNAs may also provide a means to detect asymptomatic individuals as previously demonstrated in another viral infection (Hou et al., 2017). However, potential confounding diseases that may influence the expression of multiple miRNAs requires the further evaluation of the targets found in this study (**Fig. 5**).

Recent advances in RNA chemistry and delivery systems enabled the first miRNA-based agents to enter into clinical trials several years ago (Rupaimoole and Slack, 2017). It was discovered that miR-122 increased the stability and replication of the Hepatitis C virus (HCV) through binding to the 5' end of the non-coding region that prevented degradation by the Xrn1 exoribonuclease (Jopling et al., 2005; Thibault et al., 2015). In a phase I clinical trial, a 15-nucleotide phosphorothioate DNA–locked nucleic acid anti-miRNA that is designed to inhibit miR-122 was first used and demonstrated no adverse reactions. In a subsequent phase IIa trial of 36 patients, there was a significant dose-dependent decrease in HCV load, one patient reported a grade 3 adverse event (thrombocytopenia), and only a small set of patients experienced viral rebound that may be linked to mutations of the HCV viral RNA (Janssen et al., 2013; Ottosen et al., 2015). A separate clinical trial with a N-acetyl-Dgalactosamine (GalNAc)-conjugated anti-miRNA targeting miR-122 and antiviral agents (ledipasvir and sofosbuvir) was successful in reducing viral loads in all treated patients within 4 weeks of treatment as well as sustained viral response in three patients after 76 weeks of follow-up (van der Ree et al., 2017), however subsequent treatments have been suspended due to two cases of severe jaundice. These clinical trials have demonstrated the promising potential of using anti-miRNAs to significantly reduce viral infection with limited adverse effects and the similarities with miR-2392 with SARS-CoV-2 warrant further investigations to push to clinical trials.

Presently, there remains no specific treatment option for patients presenting with severe COVID-19 disease. While vaccines provide a promising avenue towards preventing the development of these symptoms as well as curbing the infection rate, there remains an urgency to successfully develop and implement therapeutic agents to reduce severe consequences from infection and subsequent patient mortality. As the testing of antibody-based or drug targeted therapies are currently underway, the added utility of miRNAs represents a novel category of therapeutic agents that have previously shown endogenous activity to alter viral infection.

Acknowledgments: This work was supported by supplemental funds for COVID-19 research from Translational Research Institute of Space Health through NASA Cooperative Agreement NNX16AO69A (T-0404 to A.B. and T-0406 to A.C.) and further funding from KBR, Inc provided to A.B; this work used resources services, and support provided via the COVID-19 HPC Consortium (https://covid19-hpc-consortium.org/) which is a unique private-public effort to bring together government, industry, and academic leaders who are volunteering free compute time and resources, in support of COVID-19 research and resources supporting this work were provided by the NASA High-End Computing (HEC) Program through the NASA Advanced Supercomputing (NAS) Division at Ames Research Center which was awarded to A.B.; DOD W81XWH-21-1-0128 awarded to D.C.W.; NIGMS P20 GM1009005 awarded to N.A.;

Individual National Research Service Award F32-AI147587 awarded to J.M.D.; NIH/NHBLI K08 HL143271 and NIH/NHLBI R03 HL155249 awarded to R.S.H.; NIH/NCI U54 CA260543 supported R.S.H., N.M.B., M.C.W.; NSF 1956233 awarded to R.M.; A.P. was supported by Biotechnology and Biological Sciences Research Council (https://bbsrc.ukri.org/) grants BB/K004131/1, BB/F00964X/1 and BB/M025047/1, Consejo Nacional de Ciencia y Tecnología Paraguay - CONACyT (http://www.conacyt.gov.py/) grants 14-INV-088 and PINV15-315, National Science Foundation Advances in Bio Informatics (https://www.nsf.gov/) grant 1660648; D.G. and A.P. were supported by the CONACyT grant PINV20-337 and the Fundação Getulio Vargas. N.M.B. was supported by the National Center for Advancing Translational Sciences (NCATS), NIH UL1TR002489, 2KR1272005, 550KR242003.

Author contributions

Conceptualization: A.B.; Methodology: A.B.; Formal Analysis: A.B., R.M., C.V., D.T., F.J.E., C.M., C.M., J.C.S., J.T.M., J.M.D., D.G., U.S., E.S.W., A.S., J.F., V.Z., N.S., T.J.T.; Investigation: A.B., C.V., R.M., C.E.M., A.C., P.N., M.F., R.A.B., M.M., S.L.M., A.Y., T.R.A.; Sample Collection: M.M.S., M.C.W., R.S.H., N.M.B., U.C.P.C., A.D.H., J.C.; Resources: A.B., R.M., C.E.M., A.C., M.S., M.F., M.C.W.; Writing – Original Draft: A.B., J.T.M.; Writing – Review & Editing: A.B., J.T.M., F.J.E., R.J.G., W.P., M.M.S., J.M.D., J.W.G., D.W., S.B., V.Z., E.S.W., S.V.C., N.A, A.P., D.G., M.F., P.M.C., M.M., M.R.E., J.C.S., A.C., R.M., N.S., T.J.T., B.C., L.N.S., M.C.W.; Visualization: A.B., J.S.C, F.J.E, D.G., N.S., V.Z.; Supervision: A.B.; Funding Acquisition: A.B.

Declaration of Interests

The authors declare no competing interests.

Figure Legends

Figure 1. Key miRNA signature as predicted from Bronchial Alveolar Lavage Fluid (BALF) RNA-seq data in patients with COVID-19. A) Predicted upstream regulators determined through Ingenuity Pathway Analysis (IPA) consistent with the transcriptional response from differentially expressed genes (FDR<0.05; outer ring). Eight miRNAs were among the key regulators in response to COVID-19 (inner ring). **B)** Major biological responses resulting from dysregulation of this eight miRNA signature drive immune- and inflammatory-related pathways as well as mitochondrial dysfunction determined through IPA. **C)** Pathway regulation by miR-2392 from BALF RNA-seq data determined through IPA.

Figure 2. Cross-species and viral integration of miR-2392. A) The conservation of miR-2392 across species determined by UCSC Genome Browser. The boxes (■) represent aligning and conserved sequence regions. Double horizontal line (=) represents both the genome and query have unalignable sequence between regions of aligned sequence, a double-sided insertion. Single lines (-) indicate gaps that are largely due to a deletion in the genome of the first species or an insertion in the genome of the second species. **B)** The expression of MEG3, the miR-2392 host gene, in different tissues from healthy patients. **C)** Potential binding sites of miR-2392 visualized across 300 windows of 100bp length in SARS-CoV-2 genomes (NC045512.2 reference, and representative genomes for variants and lineages of concern from GISAID). The score in each

window is the average of miRanda scores for hits within that 100bp window. Three top hits are shown explicitly at the bottom of the plot.

Figure 3. Gene targets of miR-2392 in COVID-19 patients as well as mitochondrial and inflammatory genes. Volcano plots showing the differential gene expression analysis from **A)** nasopharyngeal swab and autopsy COVID-19 patient tissues from the **B)** heart, **C)** kidney, **D)** liver, **E)** lung, and **F)** lymph node from RNA-seq datasets separated by viral load. **G)** Differential gene expression analysis for all miR-2392 gene targets significantly expressed in nasopharyngeal swab and autopsy COVID-19 patient tissues. The heatmaps display the t-score statistics for comparing viral load vs negative patient sample for all samples. Main gene clusters were determined through k-mean clustering. Six main gene clusters were determined and ShinyGO (Ge et al., 2020) was utilized to determine the pathways for each cluster which are displayed on the top panel of the heatmap. miR-2392 gene targets in for **H)** mitochondrial specific genes or **I)** inflammatory genes are displayed. Differentially expressed genes are shown with at least one comparison demonstrating a significant adjusted p-value (FDR<0.05) when comparing COVID-19 patients (high, medium or low viral loads) to non-infected control patients (none). A heatmap for the miR-2392 mitochondrial gene targets from the full list of targets determined only from miRmap is available in **Fig. S1**. A heatmap for the miR-2392 inflammatory gene targets from the full list of targets determined only from miRmap is available in **Fig. S2**. **J)** Scatter plot of log_2-transformed Fold Changes in RNAs and proteins for miR-2392 targets. The chart shows a set of genes differentially expressed at the RNA level. Student's t-test, RNA p-value<= 0.05, no limitation on protein p-value. **K)** Scatter plot of log_2 transformed medians in RNAs and proteins. The orange color represents COVID-19 positive samples, grey - COVID-19 negative samples. Student's t-test is used in Fold Change calculations. The size and the opacity of the point represent log2-transformed Fold Change at the RNA level. The shape of the point represents Fold Change direction: circle - positive, triangle - negative. Pearson correlation for COVID-19 positive samples displayed in orange, for COVID-19 negative samples - in grey.

Figure 4. Increased miR-2392 expression *in vitro* mimics a COVID-19 disease phenotype. **A-F)** Volcano plots for RNA-seq results in cells overexpressing miR-2392. **G-J)** Correlation plot of RNA-seq between miR-2392 overexpression and related SARS-CoV-2 datasets. The circle size is proportional to the correlation coefficient. Statistical significance was determined using a two-tailed Student's t-test *p < 0.05, **p < 0.01, ***p < 0.001. **K-O**) Dot plots for statistically significant gene sets determined by fGSEA. NES, nominal enrichment score. **P)** and **Q)** Predicted miR-2392 targets by the MIRDIP algorithm that are downregulated in the overexpression experiments. The putative miR-2392 mRNA targets belonging to the consensus transcriptomic networks observed in SARS-CoV-2, MERS and Influenza infections of different human cells are represented in a Venn diagram in the upper part of the panel **P**.

Figure 5. Circulating miR-2392 with COVID-19 patients compared to COVID-19 negative patients. Droplet digital PCR (ddPCR) with specific primer for miR-2392 was performed on serum, urine, and nasopharyngeal swab samples (including other seasonal coronavirus samples) from COVID-19 positive and negative patients. The miRNA concentration is reported as

copies/5ng RNA. **A)** The levels of miRNA-2392 in all tissues from patients grouped as SARS-CoV-2 positive (SARS-nCoV-2) or negative (neg). Unadjusted t-tests comparing the SARS-CoV-2 positive to neg for each tissue are provided and also adjusted statistics comparing the groups with a mixed model corrected for age and sex is provided. **B)** Receiver Operating Characteristic (ROC) curve is provided for miR-2392 for each tissue comparing SARS-CoV-2 positive to negative patients. **C)** Comparing specific categories within each tissue type between COVID-19 positive and negative patients. N = COVID-19 Negative, P = COVID-19 positive, P_{int} = intubated patients, outp = outpatient, ICU = Intensive care unit/inpatient, Cold = Coronaviruses related to the common cold, NL63 = NL63 coronavirus, and CoV-2 = SARS-CoV-2. For all plots * = $p < 0.05$, ** = $p < 0.01$, and *** = $p < 0.001$. We also quantified three other miRNAs with same patient samples as comparison which were miR-1-3p (**Fig. S3**), miR-155-5p (**Fig. S4**), and miR-124-3p (**Fig. S5**).

Figure 6. Anti-miR-2393 therapeutic mitigation of SARS-CoV-2 infection with *in vitro* and *in vivo* models. A) Schematic of the design for the miR-2392 inhibitor with the FASTmer platform, the synthesis and formulation of the inhibitor, and the experimental models utilized for testing the inhibitor. **B) – D)** Anti-miR-2392 FASTmer inhibitor applied to A549 human cells infected with SARS-CoV-2 and tested for viral viability and cytotoxicity. Viral viability is inhibited by 100% with near 0% cytotoxicity. **E) – G)** Nonsense FASTmer inhibitor applied to A549 human cells infected with SARS-CoV-2 and tested for viral viability and cytotoxicity. Viral viability is inhibited by 50% with near 0% cytotoxicity. **H) – J)** Toxicity and efficacy of anti-miR-2392 FASTmer inhibitor in an *in vivo* infection hamster model. There were six treatments groups: SBCov207 by IP injection 24 hours prior to viral inoculation (IP Day -1), SBCov207 by IP injection 24 hours prior to viral inoculation and 24 hours post-viral challenge (IP Day -1, +1), SBCov207 by IN injection 24 hours prior viral inoculation (IN Day -1), SBCov207 by IN injection 24 hours prior viral inoculation and 24 hours post-viral challenge (IN Day -1, +1), and 100ul of PBS as a control treatment 24 hours prior and post-viral challenge through IN instillation (PBS IN Day -1, +1). **H)** Weights per day for each of the 5 groups pooled (n = 6 for days 1 – 3 and n = 3 for days 4 -7), and the maximum percent weight loss, observing for the two different endpoints. **I)** SARS-CoV-2 assayed by plaque assay on Vero E6 cells from oropharyngeal swabs collected on days 1, 2 and 3. N=6 for each treatment group. **J)** Histopathological total score for lung tissues at day 3; anti-miR-2392 treatments have lower scores than the PBS control. Intranasal (IN), intraperitoneal (IP).

Figure 7. Predicted impact of miR-2392 on human disease and the top-20 drug compounds predicted to affect miR-2392 expression through machine learning approach. **A)** Dot plot of diseases associated with miR-2392, as predicted from miR-2392 gene targets by miRnet. The diseases were manually curated to emphasize specific diseases and tissues. The values are plotted according to p-value, and the size of each dot represents the number of downstream gene targets for miR-2392 associated with each disease prediction. The specific cancer relationship to miR-2392 is highlighted in **Fig. S7**, relating miR-2392 expression with patient survival in a pan-cancer analysis. **B)** Barplot of scores using our matrix completion model to predict small molecules that affect miRNA expression. Higher scores indicate more predicted associations. **C)**

Barplot of the normalized connectivity map (CMAP) scores. We used transcripts induced by miR-2392 overrepresented genes to query CMAP. Higher negative scores reflect a greater reversal of the miR-2392 transcriptomic signature. Further details on model statistics and performance are found in **Figs. S8 – S10**.

Supplemental Figures and Material

The UNC COVID-19 Pathobiology Consortium is comprised of:
Shannon M Wallet[1,2], Robert Maile[2,3], Matthew C Wolfgang[2,4], Robert S Hagan[4,5], Jason R Mock[4,5], Natalie M Bowman[6], Jose L Torres-Castillo[5], Miriya K Love[5], Suzanne L Meinig[4], Will Lovell[1], Colleen Rice[5], Olivia Mitchem[1], Dominique Burgess[1], Jessica Suggs[1], Jordan Jacobs[3]

[1]Department of Oral and Craniofacial Health Sciences, UNC Adams School of Dentistry, University of North Carolina School of Medicine, Chapel Hill, NC, 27599, USA
[2]Department of Microbiology & Immunology, University of North Carolina School of Medicine, Chapel Hill, NC, 27599, USA
[3]Department of Surgery, University of North Carolina School of Medicine, Chapel Hill, NC, 27599, USA
[4]Marsico Lung Institute, University of North Carolina at Chapel Hill, Chapel Hill, NC, 27599, USA
[5]Division of Pulmonary Diseases and Critical Care Medicine, Department of Medicine, University of North Carolina, Chapel Hill, NC 27599, USA
[6]Division of Infectious Disease, School of Medicine, University of North Carolina, Chapel Hill, NC, 27599, USA

Figure S1. Mitochondrial gene targets of miR-2392 and regulated pathways. Related to Figure 3. Differential gene expression analysis for all miR-2392 mitochondrial gene targets significantly expressed in nasopharyngeal swab and autopsy COVID-19 patient tissues. The heatmaps display the t-score statistics for comparing viral load vs negative patient sample for all samples. Main gene clusters were determined through k-mean clustering. Nine main gene clusters were determined and ShinyGO (Ge et al., 2020) was utilized to determine the pathways for each cluster which are displayed on the top panel of the heatmap. Differentially expressed genes are shown with at least one comparison demonstrating a significant adjusted p-value (FDR<0.05) when comparing COVID-19 patients (high, medium or low viral loads) to non-infected control patients (none). Mir-2392 gene targets only determined from miRmap.

Figure S2. Inflammatory gene targets of miR-2392 and regulated pathways. Related to Figure 3. Differential gene expression analysis for all miR-2392 inflammatory gene targets significantly expressed in nasopharyngeal swab and autopsy COVID-19 patient tissues. The heatmaps display the t-score statistics for comparing viral load vs negative patient sample for all samples. Main gene clusters were determined through k-mean clustering. Eight main gene clusters were determined and ShinyGO (Ge et al., 2020) was utilized to determine the pathways for each cluster which are displayed on the top panel of the heatmap. Differentially expressed

genes are shown with at least one comparison demonstrating a significant adjusted p-value (FDR<0.05) when comparing COVID-19 patients (high, medium or low viral loads) to non-infected control patients (none). Mir-2392 gene targets only determined from miRmap.

Figure S3. Circulating miR-1-3p with COVID-19 patients compared to COVID-19 negative patients. Related to Figure 5. Droplet digital PCR (ddPCR) with specific primer for miR-1-3p was performed on serum, urine, and nasopharyngeal swab samples (including other seasonal coronavirus samples) from COVID-19 positive and negative patients. The miRNA concentration are reported as copies/5ng RNA. **A)** The levels of miRNA-2392 in all tissues from patients grouped as SARS-CoV-2 positive (SARS-nCoV-2) or negative (neg). Unadjusted t-tests comparing the SARS-CoV-2 positive to neg for each tissue are provided and also adjusted statistics comparing the groups with a mixed model corrected for age and sex is provided. **B)** Receiver Operating Characteristic (ROC) curve is provided for miR-1-3p for each tissue comparing SARS-CoV-2 positive to negative patients. **C)** Comparing specific categories within each tissue type between COVID-19 positive and negative patients. N = COVID-19 Negative, P = COVID-19 positive, P_{int} = intubated patients, outp = outpatient, ICU = Intensive care unit/inpatient, Cold = Coronaviruses related to the common cold, NL63 = NL63 coronavirus, and CoV-2 = SARS-CoV-2. For all plots * = $p < 0.05$, ** = $p < 0.01$, and *** = $p < 0.001$.

Figure S4. Circulating miR-155-5p with COVID-19 patients compared to COVID-19 negative patients. Related to Figure 5. Droplet digital PCR (ddPCR) with specific primer for miR-155-5p was performed on serum, urine, and nasopharyngeal swab samples (including other seasonal coronavirus samples) from COVID-19 positive and negative patients. The miRNA concentration are reported as copies/5ng RNA. **A)** The levels of miRNA-2392 in all tissues from patients grouped as SARS-CoV-2 positive (SARS-nCoV-2) or negative (neg). Unadjusted t-tests comparing the SARS-CoV-2 positive to neg for each tissue are provided and also adjusted statistics comparing the groups with a mixed model corrected for age and sex is provided. **B)** Receiver Operating Characteristic (ROC) curve is provided for miR-155-5p for each tissue comparing SARS-CoV-2 positive to negative patients. **C)** Comparing specific categories within each tissue type between COVID-19 positive and negative patients. N = COVID-19 Negative, P = COVID-19 positive, P_{int} = intubated patients, outp = outpatient, ICU = Intensive care unit/inpatient, Cold = Coronaviruses related to the common cold, NL63 = NL63 coronavirus, and CoV-2 = SARS-CoV-2. For all plots * = $p < 0.05$, ** = $p < 0.01$, and *** = $p < 0.001$.

Figure S5. Circulating miR-124-3p with COVID-19 patients compared to COVID-19 negative patients. Related to Figure 5. Droplet digital PCR (ddPCR) with specific primer for miR-124-3p was performed on serum, urine, and nasopharyngeal swab samples (including other seasonal coronavirus samples) from COVID-19 positive and negative patients. The miRNA concentration are reported as copies/5ng RNA. For miR-124-3p, the copies/5ng were either equal to 0 or at extremely low levels close to 0 copies/5ng. To try to determine any statistical differences we categorized the groups as ND = Not Determined which are all 0 values or D = Determined which are values > 0 for both N = negative (open symbols) and P = COVID-19 positive patients samples (closed symbols). The number of patients for each column is shown

above the points. No significant differences were observed for any of the sample for miR-124-3p.

Figure S6. miR-2392 expression pan-cancer survival analysis. Related to Figure 7. Kaplan Meier patient survival plots for miR-2392 expression in a pan-cancer analysis was determined utilizing The Kaplan Meier plotter (Nagy et al., 2021). The plots were separated with the top row being cancers which patients had significantly poor survival with high expression of miR-2392, the middle row being cancers which patients had poor survival (but not significant) with high expression of miR-2392, and the bottom row being cancers which patients had significantly better survival with high expression of miR-2392.

Figure S7. Small molecules-miRNA dataset statistics Related to Figure 7. (Left) Number of small molecules associated to miRNAs. (Right) Number of miRNAs associated to small molecules.

Figure S8. Performance of our method at predicting missing small molecule-miRNA interactions. Related to Figure 7. (Top) The mean value of the Receiver Operating Curve (ROC) is shown for a ten-fold cross-validation experiment (dark blue). 95% confidence interval is also shown (light blue). (Bottom) The mean value of the Precision-Recall Curve (PRC) is shown for a ten-fold cross-validation experiment (dark salmon). 95% confidence interval is also shown (light salmon).

Figure S9. Performance of our method at predicting missing small molecule-miRNA interactions when controlling for data imbalance. Related to Figure 7. (Top) Area Under the Receiver Operating Curve (AUROC) was obtained in a ten-fold cross-validation experiment for varying values of the negative to positive label ratio in the test set. (Bottom) Area Under the Precision-Recall Curve (AUROC) was obtained in a ten-fold cross-validation experiment for varying values of the negative to positive label ratio in the test set.

Table S1. Annealing temperatures for miRNA primers, related to methods and Figure 5. Temperatures used for droplet digital PCR to quantify each miRNA target.

STAR Methods

RESOURCE AVAILABILITY

Lead Contact

Further information and requests for resources and reagents should be directed to and will be fulfilled by the Lead Contact, Afshin Beheshti (afshin.beheshti@nasa.gov).

Materials Availability

This study did not generate new unique reagents.

Data and Code Availability

The published article includes all datasets generated and analyzed during this study. Processed bulk RNA-seq data is available online (https://covidgenes.weill.cornell.edu/). RNA-Seq alignment script for BALF samples and SHSY-5Y cells studies are attached. Limma script for SHSY5Y studies is attached.

EXPERIMENTAL MODEL AND SUBJECT DETAILS

Human serum and nasopharyngeal swab sample collection for ddPCR

All plasma and nasal swab samples from those with COVID-19 infection, seasonal coronavirus infection, and controls were collected from inpatients at the University of Maryland Medical Center, in Baltimore, USA, between March and May of 2020. Sample collection obtained through informed consent waiver, which was approved by the University of Maryland, Baltimore IRB.

For serum samples, N=10 samples from COVID-19 intubated patients, COVID-19 outpatients, and COVID-19 negative patients were obtained. An equal distribution of N=5 males and females were used for each group. Also, an equal age distribution of patients from 27 to 85 years old was utilized for each group.

For the nasopharyngeal samples the following patient samples were obtained: N=10 SARS-CoV-2 positive patients, N=6 common cold coronavirus samples, and N=6 Coronavirus NL63 samples. For the common cold coronavirus samples the breakdown was the following for the specific viruses: N=2 Coronavirus 229E, Coronavirus HKU1, and N=2 Coronavirus OC43.

Human nasopharyngeal swab sample collection for RNA-seq analysis

Patient specimens were processed as described in Butler et al., 2020 (Butler et al., 2021). Briefly, nasopharyngeal swabs were collected using the BD Universal Viral Transport Media system (Becton, Dickinson and Company, Franklin Lakes, NJ) from symptomatic patients. Total Nucleic Acid (TNA) was extracted from using automated nucleic acid extraction on the QIAsymphony and the DSP Virus/Pathogen Mini Kit (Qiagen).

Human autopsy tissue collection for RNA-seq analysis

The full methods of the patient sample collection from the autopsy patients are currently available in the Park et al. (Park et al., 2021). All autopsies are performed with consent of next of kin and permission for retention and research use of tissue. Autopsies were performed in a negative pressure room with protective equipment including N-95 masks; brain and bone were not obtained for safety reasons. All fresh tissues were procured prior to fixation and directly into Trizol for downstream RNA extraction. Tissues were collected from lung, liver, lymph nodes, kidney, and the heart as consent permitted. For GeoMx, RNAscope, trichrome and histology tissue sections were fixed in 10% neutral buffered formalin for 48 hours before processing and sectioning. These cases had a post-mortem interval of less than 48 hours. For bulk RNA-seq tissues, post-mortem intervals ranged from less than 24 hours to 72 hours (with 2 exceptions - one at 4 and one at 7 days - but passing RNA quality metrics) with an average of 2.5 days. All deceased patient remains were refrigerated at 4ºC prior to autopsy performance.

Human urine sample collection

Urine was collected from patients and volunteers at the University of North Carolina at Chapel Hill. All patients provided informed consent prior to participation in IRB-approved research protocols (UNC IRB: 20-0822 [RHS] and 20-0792 [NMB]). Mid-stream urine of outpatients and non-critically ill patients was collected by the clean catch method. Urine of intubated critically ill patients was collected from a port on the Foley catheter. Urine was aliquoted into 5 ml aliquots and stored at -80°C.

Urine aliquots were thawed, and microRNA was extracted from 1 ml per sample using Norgen Urine microRNA Purification Kit (Cat. 29000). Microalbumin and creatinine levels were assessed using Microalbumin 2-1 Combo strips (CLIAwaived Inc, cat# URS-2M).

Cell lines used for miR-2392 mimic experiments

Human SH-SY5Y cells were obtained from the ATCC and grown in Minimum Essential Medium (Gibco) / 10% FBS (Invitrogen) /1% MEM Non Essential Amino Acids (Gibco) / 1%GlutaMAX -l (Gibco). Cells were plated in 3.5 cm dishes and incubated with miR-2392 or control lentivirus particles (MOI 1) for 48h. Cells were harvested and lysed in Trizol reagent and RNA was extracted following manufacturers protocol (Invitrogen).

COVID-19 hamster model

Male Syrian hamsters 6-8 weeks old were utilized for efficacy studies with anti-miR-2392 FASTmer treatment. Three hamsters were used for each experimental group for a total of 30 hamsters with 10 treatment groups. Hamsters were infected with 10^5 pfu of SARS-CoV-2. There were 5 major treatment groups (N=6 per group) with two endpoints at day 3 or 7 post-viral challenge (N=3 per endpoint). Groups 1 and 3 were given the FASTmer treatment by IP injection while groups 2 and 4 were given by IN instillation under ketamine-xylazine anesthesia. Groups 1 and 2 were given single FASTmer treatment 24 hours before viral challenge. Groups 3 and 4 were given two doses of FASTmers at 24 hours before and 24 hours after viral challenge. The control group 5 was treated with PBS 24 hours prior to and 24 hours following viral challenge by IN instillation.

Treatment efficacy was assessed in multiple ways: 1) Change in daily body weight, 2) oropharyngeal shedding of virus on days 1-3 from all groups post-challenge assayed by plaque assay on Vero E6 cells (PFU/swab), 3) tissue burden of the virus at necropsy on day 3 from 2 lung tubes and turbinates assayed by plaque assay (PFU/100mg), and 4) histopathologic scoring on lungs and turbinates from all hamsters; the histopathological score for individual tissues, inflammation score from the interstitial lung inflammation, and total histopathological scores/assessment was made.

The dose of anti-miR-2392 that was used was calculated to raise blood levels to 10 μM if it were given intravenously. The molecular weight of anti-miR-2392 is 15,804. Assuming that hamsters weigh 120 grams and have 8% of body weight as blood, blood volume was approximately 0.01 liters. The dose per hamster was 1.58 mg in a 100 μl volume from an anti-miR-2392 solution.

In vitro viral screening model

A549-ACE2 cells, gifted by Dr. Brad Rosenberg (MSSM), were maintained in DMEM (Quality Biological, Gaithersburg, MD; #112-014-101) + 10% Fetal Bovine Serum (Gibco; #26140079) + 1% Penicillin-Streptomycin (Gemini Bio; #400-109). The day prior to treatment, 5,000 A549-ACE2 cells were plated per well in 96-well plates. MiR-2932 was diluted in duplicate in A549-ACE2 media to a starting concentration of 20μM (Run 1) or 22μM (Runs 2 and 3), and then an 8-point 1:2 dilution series was prepared. Media was removed from cells and 90μL of each dilution was transferred to the cells. The plates were incubated for 2 hours at 37°C before being infected with an M.O.I. of 0.1 SARS-CoV-2 WA-1 (provided by Dr. Natalie Thornburg at the Centers for Disease Control and Prevention). Parallel plates were also run and left uninfected to monitor toxicity. Since Runs 2 and 3 were run simultaneously, a single toxicity plate was run for both. All plates were incubated at 37°C for 72 hours before being analyzed via Cell Titer Glo (Promega, Madison, WI; #G7573). Cell viability was compared to uninfected, untreated cells and infected, untreated cells.

METHOD DETAILS

miRNA extraction for Droplet Digital PCR (ddPCR)

MiRNA extractions from serum were carried out using the Qiagen miRNeasy serum/plasma kit (#217184). MiRNA extractions from urine samples were carried out using Norgen urine microRNA Purification Kit (Cat. 29000, Norgen Bioteck Corp. Thorold, ON, Canada). Quantitation of miRNA samples was done using a NanoDrop 2000 Spectrophotometer (ThermoFisher Scientific).

cDNA generation and ddPCR

First, cDNA was synthesized from miRNA samples using the Qiagen miRCURY LNA RT Kit (Cat. 339340) using a concentration of 5ng/μl for the miRNA per sample. Next, samples were mixed with a 1:20 dilution of the generated cDNA with the BioRad QX200 ddPCR Evagreen Supermix (Cat. 1864034) and the appropriate miRNA primers from miRCURY LNA miRNA PCR Assays (Qiagen). BioRad QX200 Automated Droplet Generator (Cat. 1864101) was used to create emulsion droplets. With the C1000 Touch™ Thermal Cycler with 96–Deep Well Reaction Module (Bio-Rad) the following PCR reaction was used for all the primers: 1 cycle 95°C for 5 min, 40 cycles of 95°C for 30 sec and 58°C for 1 min (the annealing temperature can change depending on the primer), 1 cycle of 4°C for 5 min, and 1 cycle of 90°C for 5 min. Not all miRNA primers sets for ddPCR will have the same annealing temperature, so optimizing the annealing temperature is required for each primer set. Their respective annealing temperatures are found in **Table S1**. Finally, the QX200™ Droplet Digital™ PCR System (Bio-Rad) quantified the amount of miRNA for each primer set per sample. QuantaSoft software (Bio-Rad) generated the data for each primer set and sample. The same threshold setting was used for all samples per primer set. The concentration (miRNA copies/μl) value generated by QuantaSoft was converted to miRNA copies/ng of serum. These values were used for all miRNA analysis. For all analysis the miRNA concentrations were $\log_2(x+1)$ transformed to allow for easy comparison between miRNAs and samples.

Publicly available Bronchial Alveolar Lavage Fluid (BALF) COVID-19 RNA-sequencing data

Fastq files were downloaded from SRA (NCBI BioProject PRJNA605907 (Shen et al., 2020) and NCBI BioProject PRJNA390194 (Ren et al., 2018)). Fastq data files were trimmed using TrimGalore v (0.6.4) with a quality cutoff of 30. Data were then aligned using STAR (v2.7.3) two pass mode to the Human reference genome (GRCh38 v99 downloaded 04-27-2020). Unaligned data were written to a fastq file, and then realigned to the GRCh38 reference genome using Bowtie 2 (v2.3.4.1), and output sam file converted to a bam file using samtools (v1.7). The resultant Bam files were merged, sorted, and read groups added using picard tools (v2.21.3) (script in supplemental data).

Publicly available RNA-seq data: A549, Calu-3, NHBE, and COVID-19 lung biopsy

Raw RNA-seq read counts from the publication by Blanco-Melo *et al.* for the A549, Calu-3, and NHBE cell lines as well as post-mortem lung biopsies from two COVID-19 patients were downloaded from the Gene Expression Omnibus (series accession GSE147507) (Blanco-Melo et al., 2020).

RNA-seq of Nasopharyngeal Swab COVID-19 patient samples

RNA isolation and library preparation is fully described in Butler, et al. (Butler et al., 2021). Briefly, library preparation on the all nasopharyngeal swab samples' total nucleic acid (TNA) were treated with DNAse 1 (Zymo Research, Catalog # E1010). Post-DNAse digested samples were then put into the NEBNext rRNA depletion v2 (Human/Mouse/Rat), Ultra II Directional RNA (10 ng), and Unique Dual Index Primer Pairs were used following the vendor protocols from New England Biolabs. Kits were supplied from a single manufacturer lot. Completed libraries were quantified by Qubit or equivalent and run on a Bioanalyzer or equivalent for size determination. Libraries were pooled and sent to the WCM Genomics Core or HudsonAlpha for final quantification by Qubit fluorometer (ThermoFisher Scientific), TapeStation 2200 (Agilent), and qRT-PCR using the Kapa Biosystems Illumina library quantification kit.

RNA-seq of COVID-19 autopsy tissue samples

RNA isolation and library preparation is fully described in Park, et al. (Park et al., 2021). Briefly, autopsy tissues were collected from lung, liver, lymph nodes, kidney, and the heart and were placed directly into Trizol, homogenized and then snap frozen in liquid nitrogen. At least after 24 hours these tissue samples were then processed via standard protocols to isolate RNA. New York Genome Center RNA sequencing libraries were prepared using the KAPA Hyper Library Preparation Kit + RiboErase, HMR (Roche) in accordance with manufacturer's recommendations. Briefly, 50-200ng of Total RNA were used for ribosomal depletion and fragmentation. Depleted RNA underwent first and second strand cDNA synthesis followed by adenylation, and ligation of unique dual indexed adapters. Libraries were amplified using 12 cycles of PCR and cleaned-up by magnetic bead purification. Final libraries were quantified using fluorescent-based assays including PicoGreen (Life Technologies) or Qubit Fluorometer (Invitrogen) and Fragment Analyzer (Advanced Analytics) and sequenced on a NovaSeq 6000 sequencer (v1 chemistry) with 2x150bp targeting 60M reads per sample.

miR-2392 mimic experiments in SH-SY5Y cells and RNA-seq

RNA was dissolved in nuclease free water and concentration determined spectrometrically at 260nm using a Biotek plate reader (Biotek). 500ng RNA was used as input for a whole transcriptome library preparation (ThermoFisher Total RNA). Libraries were quantified using a bioanalyzer chip reader (nanoDNA chips: Aglient Technologies) and diluted to 100 pM final concentration. Barcoded libraries were combined and use to seed a OneTouch bead templating reaction (OneTouch2). Cloned libraries were enriched and loaded on 540 Ion Torrent chips. Data were sequenced using the Ion Torrent RNA-seq workflow. Unaligned Bam files were converted to fatsq and aligned to the Grch 38 reference genome using STAR Two pass approach (Dobin paper) to create gene count tables as described in Overbery et al. (Overbey et al., 2021) (script in supplementary).

Anti-miR-2392 FASTmer inhibitor design and construction

The FAST (Facile Accelerated Specific Therapeutics) platform was used to design FASTmer inhibitors, which are composed of a nanobiohydrd molecule based on antisense peptide nucleic acid (PNA) moiety conjugated to nanoparticle for improved delivery and membrane transport. The PNA moiety was chosen to be 15 bases long (in order to maximize both solubility and specificity), which yielded six potential target sequences within the 20-nucleotide mature human miR-2392. These potential targets were screened using FAST for solubility, self-complementing sequences, and off-targeting within the human genome (GCF_000001405.26) and SARS-CoV-2 viral genome (NC_045512). The antisense sequence complementing miR-2392 nucleotides 2 to 16 (TCTCACCCCCATCCT) was chosen in order to minimize off-targeting while maximizing coverage of the miR-2392 seed region. The FASTmer was synthesized (with an N-terminal histidine tag and a 2-(2-(2-aminoethoxy)ethoxy)acetic acid linker) on an Apex 396 peptide synthesizer (AAPPTec, LLC) with solid-phase Fmoc chemistry. Fmoc-PNA monomers were obtained from PolyOrg Inc., with A, C, and G monomers protected with Bhoc groups. Following synthesis, the peptides were conjugated with nanoparticles and purified via size-exclusion filtration. Conjugation and concentration of the purified solution was monitored through measurement of absorbance at 260 nm (for detection of PNA) and 400 nm (for quantification of gold nanoparticles).

QUANTIFICATION AND STATISTICAL ANALYSIS

Analysis of BALF RNA-seq data

Bam files were imported into Partek Genome Studio v7.0, and gene expression values quantified vs the Grch38 reference annotation guide (Ensembl v99). Samples with fewer than 2 million aligned reads were excluded from further analysis. Genes with fewer than 10 reads in 25% of samples were excluded, and differential gene expression determined using ANOVA with infection status as contrast. Differentially expressed gene files were used in GSEA and IPA to determine biological significance and pathways being regulated.

Analysis of Nasopharyngeal Swab RNA-seq data

The nasopharyngeal swab samples were analyzed comparing COVID-19 viral infection to the negative patients and was as previously described in Butler et al. (Butler et al., 2021) and the DESeq2 (Love et al., 2014) was utilized to generate the differential expression data. Heatmaps were displayed using pheatmap (Kolde, 2015). Volcano plots were made use R program EnhancedVolcano (Blighe et al., 2018).

Analysis of Autopsy RNA-seq data

The full methods of the analysis from the autopsy patients is currently available in the Park et al. (Park et al., 2021). Briefly, RNA-seq data was processed through the nf-core/rnaseq pipeline (Ewels et al., 2020). This workflow involved adapter trimming using Trim Galore! (https://github.com/FelixKrueger/TrimGalore), read alignment with STAR (Dobin et al., 2013), gene quantification with Salmon (Patro et al., 2017), duplicate read marking with Picard MarkDuplicates (https://github.com/broadinstitute/picard), and transcript quantification with StringTie (Kovaka et al., 2019). Other quality control measures included RSeQC, Qualimap, and dupRadar. Alignment was performed using the GRCh38 build native to nf-core and annotation was performed using Gencode Human Release 33 (GRCH38.p13). FeatureCounts reads were normalized using variance-stabilizing transform (vst) in DESeq2 package in R for visualization purposes in log-scale (Love et al., 2014). Differential expression of genes were calculated by DESeq2. Differential expression comparisons were done as either COVID+ cases versus COVID- controls for each tissue specifically, correcting for sequencing batches with a covariate where applicable, or pairwise comparison of viral levels from the lung as determined by nCounter data. Volcano plots were made use R program EnhancedVolcano (Blighe et al., 2018).

Analysis Combining Autopsy and Nasopharyngeal Swab RNA-seq data

To combine the results from the autopsy and nasopharyngeal swab RNA-seq data, we utilized the t-score values from the DESeq2 analysis. Heatmaps were displayed using pheatmap (Kolde, 2015).

Gene Set Enrichment Analysis (GSEA)

For pathway analysis on the miR-2392 targets (**Fig. 3**) we utilized ShinyGO (Ge et al., 2020) to determine the significantly regulated pathways for each main cluster in the heatmap. The clustering was determined through k-mean statistics.

For pathway analysis on the miR-2392 mimic RNA-seq data, we utilized fast Gene Set Enrichment Analysis (fGSEA) (Korotkevich et al., 2021). Pathway analysis was done comparing miR-2392 mimics to all controls and the ranked list of genes were defined by the t-score statistics. The statistical significance was determined by 1000 permutations of the genesets (Subramanian et al., 2005).

Analysis of proteomic and transcriptomic blood datasets from COVID-19 patients

For the analysis of the miR-2392 targets in the blood tissue, we downloaded whole blood transcriptome data and plasma proteome data from The COVIDome Explorer Researcher Portal (Sullivan et al., 2021). For Transcriptome data we used the following filters: Category "Effect of COVID-19 status", Platform "Blood", Statistical test "Student's t-test", Adjustment method

"none", Sex "male" and "female", Age Group "All". For Proteome data we used the following filters: Category "Effect of COVID-19 status", Platform "SOMAscan", Statistical test "Student's t-test", Adjustment method "none", Sex "male" and "female", Age Group "All". We created the list of the intersecting genes from both datasets. We analyzed the list using RStudio Desktop 1.3.1093 (RStudio Team (2020). RStudio: Integrated Development Environment for R. RStudio, PBC, Boston, MA URL http://www.rstudio.com/), and visualized data using ggplot2 version 3.3.2 (Wickham, 2016) and ggrepel version 0.8.2 (https://ggrepel.slowkow.com/).

Analysis of Monocyte RNA-seq data

The monocyte COVID-19 RNA-Seq data, published under the accession GSE159678 (Rother et al., 2020), was downloaded from SRA and gene expression was quantified using Salmon's selective alignment approach (Srivastava et al., 2020). The RNA-Seq processing pipeline was implemented using pyrpipe (Singh et al., 2021) (https://github.com/urmi-21/pyrpipe/tree/master/case_studies/Covid_RNA-Seq). Exploratory data analysis and differential expression analysis were performed using MetaOmGraph (Singh et al., 2020).

Analysis of A549, Calu-3, NHBE, and COVID lung biopsy data

Each data series was normalized and filtered for low-expressed genes (counts<1). Cell culture samples treated with SARS-CoV-2 were compared to untreated controls and COVID-19-positive patient samples were compared to healthy lung biopsies. Differentially expressed genes were determined from the R-program Limma-Voom (Ritchie et al., 2015) using a linear model with weighted least squares for each gene and the false discovery rate adjusted p-values were calculated.

Analysis of miR-2392 mimic RNA-seq data

Differential gene expression was determined using LIMMA-voom (Ritchie et al., 2015). Data were filtered to ensure data contained at least 5 million aligned reads, and average gene counts of > 10. Cell treatments we used as contrasts for differentially expressed gene calculations. These results were then uploaded to GSEA for further analysis. (R script in supplementary section)

Conservation of miR-2392 between species

To determined conservation of miR-2392 among different species we utilized UCSC Genome Browser (Kent et al., 2002). Hsa-miR-2392 was entered as an input and a select of species was used to compare which included common species that are currently used in SARS-CoV-2 *in vivo* studies (i.e. mice, ferrets, and hamsters). We also chose primates and other animals to provide a wide spectrum of species to observe conservation of miR-2392. Lastly, the USCS Genome Browser provides the host gene for miR-2392 (i.e. MEG3) and redirects to GTEx (Consortium, 2020) to provide a plot of MEG3 levels based on RNA-seq data on normal tissues.

Mapping miR-2392 sequence to SARS-CoV-2 sequences

To explore potential binding sites for miR-2392 we used miRanda software (Enright et al., 2003) to identify all potential binding sites with respect to the SARS-CoV-2 reference genome

(Wuhan-Hu-1; NC045512.2) and representative genomes from lineages of concern. The lineages of concern were selected from Global Initiative on Sharing All Influenza Data (GISAID) with each lineage being represented by 14 recent genomes.

In silico predictions of genes from miRNAs

Through the use of a Cytoscape (Shannon et al., 2003) plug-in called ClueGo/CluePedia (Bindea et al., 2013), we were able to predict genes targeted by the miRNAs determined. This involved entering all miRNAs in ClueGo and allowing the software to determine the top 50 genes that were significantly regulated and connected to the miRNAs. The predictions only reflect the functions that will be regulated by the miRNAs and do not show whether the function will be activated or inhibited. Lastly, miRNet 2.0 was utilized to predict the diseases and pathways that are associated with the miRNAs (Chang et al., 2020a). This was plotted as a dot utilizing the R-program ggplot2 (v3.2.1) (Wickham, 2016).

ddPCR analysis of miRNA levels in patient samples

First, we normalized the amount of each miRNA measured per body location (nasal, serum, and urine) using the general logarithm transformation. We compared miRNA levels in samples from patients either positive or negative for SARS-nCoV-2 using the student's t-test (unadjusted) as well as controlling for sex and age using least squares adjustment. Next, we generated receiver operating characteristic curves from each body location to show the performance of a classification model (SARS-nCoV-2 positive versus negative) at all classification thresholds using the absolute, non-transformed levels (miRNA copies per 5 ng RNA). Finally, we performed a subanalysis on each location to compare the variance of each miRNA in SARS-nCoV-2 negative patients compared to other patient groups. For serum and nasal samples, 1-way ANOVA was used to identify variation associated with the patient classification. For urine samples, 2-way ANOVA was used with location (outpatient versus inpatient) and SARS-nCoV-2 positivity as the main factors. If the ANOVA yielded a $P < 0.05$, Dunnett's post-test was used to compare subgroup means to the negative patient sample mean.

Computational drug repositioning model

Using the SM2miR database (Liu et al., 2013), we assembled an $n \times m$ binary matrix (X) containing 3,593 associations between small molecules ($n = 213$, rows) and miRNAs ($m = 1,519$, columns). Each matrix entry (X_{ij}) was assigned a value of 1 where a small molecule is known to be associated to miRNA, and was 0 otherwise. The chemical notation as a simplified molecular input line entry system (SMILES) was obtained for each small molecule from PubChem. We then calculated the 2D Tanimoto chemical similarity between pairs of small molecules using the MACCS key binary fingerprints with RDKit (RDKit: Open-source cheminformatics; http://www.rdkit.org). Similarly, for each miRNA, we obtained its sequence from miRbase (Kozomara et al., 2019) and computed sequence similarity between miRNAs as the score of their Needleman-Wunsch alignment. We used the binary matrix, together with the chemical and sequence similarities, as input to our state-of-the-art drug target prediction model to predict missing associations in X (Galeano et al., 2021). The model parameters where: p = ½ ,

β_{Chem} = 1, and α_{seq} = 0. To assess the prediction performance of the model, we performed ten-fold cross-validation simulations.

References

Allegra, L., Dal Sasso, M., Bovio, C., Massoni, C., Fonti, E., and Braga, P.C. (2002). Human neutrophil oxidative bursts and their in vitro modulation by different N-acetylcysteine concentrations. Arzneimittelforschung *52*, 669-676.

Ardestani, A., and Azizi, Z. (2021). Targeting glucose metabolism for treatment of COVID-19. Signal Transduct Target Ther *6*, 112.

Asai, A., Konno, M., Ozaki, M., Otsuka, C., Vecchione, A., Arai, T., Kitagawa, T., Ofusa, K., Yabumoto, M., Hirotsu, T., *et al.* (2020). COVID-19 Drug Discovery Using Intensive Approaches. Int J Mol Sci *21*.

Aunins, T.R., Erickson, K.E., and Chatterjee, A. (2020). Transcriptome-based design of antisense inhibitors potentiates carbapenem efficacy in CRE Escherichia coli. Proc Natl Acad Sci U S A *117*, 30699-30709.

Aykin-Burns, N., Franklin, E.A., and Ercal, N. (2005). Effects of N-acetylcysteine on lead-exposed PC-12 cells. Arch Environ Contam Toxicol *49*, 119-123.

Baden, L.R., El Sahly, H.M., Essink, B., Kotloff, K., Frey, S., Novak, R., Diemert, D., Spector, S.A., Rouphael, N., Creech, C.B., *et al.* (2021). Efficacy and Safety of the mRNA-1273 SARS-CoV-2 Vaccine. N Engl J Med *384*, 403-416.

Bartoszewski, R., Dabrowski, M., Jakiela, B., Matalon, S., Harrod, K.S., Sanak, M., and Collawn, J.F. (2020). SARS-CoV-2 may regulate cellular responses through depletion of specific host miRNAs. Am J Physiol Lung Cell Mol Physiol *319*, L444-L455.

Bindea, G., Galon, J., and Mlecnik, B. (2013). CluePedia Cytoscape plugin: pathway insights using integrated experimental and in silico data. Bioinformatics *29*, 661-663.

Bindea, G., Mlecnik, B., Hackl, H., Charoentong, P., Tosolini, M., Kirilovsky, A., Fridman, W.H., Pages, F., Trajanoski, Z., and Galon, J. (2009). ClueGO: a Cytoscape plug-in to decipher functionally grouped gene ontology and pathway annotation networks. Bioinformatics *25*, 1091-1093.

Blanco-Melo, D., Nilsson-Payant, B.E., Liu, W.C., Uhl, S., Hoagland, D., Moller, R., Jordan, T.X., Oishi, K., Panis, M., Sachs, D., *et al.* (2020). Imbalanced Host Response to SARS-CoV-2 Drives Development of COVID-19. Cell *181*, 1036-1045 e1039.

Blighe, K., Rana, S., and Lewis, M. (2018). EnhancedVolcano: Publication-ready volcano plots with enhanced colouring and labeling. https://github.com/kevinblighe/EnhancedVolcano.

Butler, D., Mozsary, C., Meydan, C., Foox, J., Rosiene, J., Shaiber, A., Danko, D., Afshinnekoo, E., MacKay, M., Sedlazeck, F.J., *et al.* (2021). Shotgun transcriptome, spatial omics, and isothermal profiling of SARS-CoV-2 infection reveals unique host responses, viral diversification, and drug interactions. Nat Commun *12*, 1660.

Carboni, E., Carta, A.R., and Carboni, E. (2020). Can pioglitazone be potentially useful therapeutically in treating patients with COVID-19? Med Hypotheses *140*, 109776.

1329 Carfi, A., Bernabei, R., Landi, F., and Gemelli Against, C.-P.-A.C.S.G. (2020). Persistent
1330 Symptoms in Patients After Acute COVID-19. JAMA *324*, 603-605.

1331 Carrico, C., Meyer, J.G., He, W., Gibson, B.W., and Verdin, E. (2018). The Mitochondrial
1332 Acylome Emerges: Proteomics, Regulation by Sirtuins, and Metabolic and Disease Implications.
1333 Cell Metab *27*, 497-512.

1334 Centa, A., Fonseca, A.S., Ferreira, S., Azevedo, M.L.V., Vaz de Paula, C.B., Nagashima, S.,
1335 Machado-Souza, C., Miggiolaro, A., Baena, C.P., de Noronha, L., *et al.* (2020). Deregulated
1336 miRNA expression is associated with endothelial dysfunction in post-mortem lung biopsies of
1337 COVID-19 patients. Am J Physiol Lung Cell Mol Physiol.

1338 Chang, L., Zhou, G., Soufan, O., and Xia, J. (2020a). miRNet 2.0: network-based visual
1339 analytics for miRNA functional analysis and systems biology. Nucleic Acids Res.

1340 Chang, L., Zhou, G., Soufan, O., and Xia, J. (2020b). miRNet 2.0: network-based visual
1341 analytics for miRNA functional analysis and systems biology. Nucleic Acids Res *48*, W244-
1342 W251.

1343 Chen, J., Yao, D., Li, Y., Chen, H., He, C., Ding, N., Lu, Y., Ou, T., Zhao, S., Li, L., *et al.*
1344 (2013). Serum microRNA expression levels can predict lymph node metastasis in patients with
1345 early-stage cervical squamous cell carcinoma. Int J Mol Med *32*, 557-567.

1346 Chen, Y., and Wang, X. (2020). miRDB: an online database for prediction of functional
1347 microRNA targets. Nucleic Acids Res *48*, D127-D131.

1348 Condorelli, G., Latronico, M.V., and Dorn, G.W., 2nd (2010). microRNAs in heart disease:
1349 putative novel therapeutic targets? Eur Heart J *31*, 649-658.

1350 Consortium, G.T. (2020). The GTEx Consortium atlas of genetic regulatory effects across human
1351 tissues. Science *369*, 1318-1330.

1352 Dickey, L.L., Worne, C.L., Glover, J.L., Lane, T.E., and O'Connell, R.M. (2016). MicroRNA-
1353 155 enhances T cell trafficking and antiviral effector function in a model of coronavirus-induced
1354 neurologic disease. J Neuroinflammation *13*, 240.

1355 Dobin, A., Davis, C.A., Schlesinger, F., Drenkow, J., Zaleski, C., Jha, S., Batut, P., Chaisson,
1356 M., and Gingeras, T.R. (2013). STAR: ultrafast universal RNA-seq aligner. Bioinformatics *29*,
1357 15-21.

1358 Dweep, H., and Gretz, N. (2015). miRWalk2.0: a comprehensive atlas of microRNA-target
1359 interactions. Nat Methods *12*, 697.

1360 Edmonds, C.E., Zuckerman, S.P., and Conant, E.F. (2021). Management of Unilateral Axillary
1361 Lymphadenopathy Detected on Breast MRI in the Era of Coronavirus Disease (COVID-19)
1362 Vaccination. AJR Am J Roentgenol.

1363 Eller, K.A., Aunins, T.R., Courtney, C.M., Campos, J.K., Otoupal, P.B., Erickson, K.E.,
1364 Madinger, N.E., and Chatterjee, A. (2021). Facile accelerated specific therapeutic (FAST)
1365 platform develops antisense therapies to counter multidrug-resistant bacteria. Commun Biol *4*,
1366 331.

1367 Enomoto, Y., Takagi, R., Naito, Y., Kiniwa, T., Tanaka, Y., Hamada-Tsutsumi, S., Kawano, M.,
1368 Matsushita, S., Ochiya, T., and Miyajima, A. (2017). Identification of the novel 3' UTR
1369 sequences of human IL-21 mRNA as potential targets of miRNAs. Sci Rep *7*, 7780.

Enright, A.J., John, B., Gaul, U., Tuschl, T., Sander, C., and Marks, D.S. (2003). MicroRNA targets in Drosophila. Genome Biol *5*, R1.

Ewels, P.A., Peltzer, A., Fillinger, S., Patel, H., Alneberg, J., Wilm, A., Garcia, M.U., Di Tommaso, P., and Nahnsen, S. (2020). The nf-core framework for community-curated bioinformatics pipelines. Nat Biotechnol *38*, 276-278.

Fan, S., Tian, T., Chen, W., Lv, X., Lei, X., Zhang, H., Sun, S., Cai, L., Pan, G., He, L., *et al.* (2019). Mitochondrial miRNA Determines Chemoresistance by Reprogramming Metabolism and Regulating Mitochondrial Transcription. Cancer research *79*, 1069-1084.

Feng, L., Yin, Y.Y., Liu, C.H., Xu, K.R., Li, Q.R., Wu, J.R., and Zeng, R. (2020). Proteome-wide Data Analysis Reveals Tissue-specific Network Associated with SARS-CoV-2 Infection. J Mol Cell Biol.

Friedman, R.C., Farh, K.K., Burge, C.B., and Bartel, D.P. (2009). Most mammalian mRNAs are conserved targets of microRNAs. Genome Res *19*, 92-105.

Galeano, D., Noto, S., Jimenez, R., and Paccanaro, A. (2021). Interpretable Drug Target Predictions using Self-Expressiveness. bioRxiv, 2021.2003.2001.433365.

Ge, S.X., Jung, D., and Yao, R. (2020). ShinyGO: a graphical gene-set enrichment tool for animals and plants. Bioinformatics *36*, 2628-2629.

Gharebaghi, R., Heidary, F., Moradi, M., and Parvizi, M. (2020). Metronidazole; a Potential Novel Addition to the COVID-19 Treatment Regimen. Arch Acad Emerg Med *8*, e40.

Griffin, R.J., Monzen, H., Williams, B.W., Park, H., Lee, S.H., and Song, C.W. (2003). Arsenic trioxide induces selective tumour vascular damage via oxidative stress and increases thermosensitivity of tumours. Int J Hyperthermia *19*, 575-589.

Gudbjartsson, D.F., Norddahl, G.L., Melsted, P., Gunnarsdottir, K., Holm, H., Eythorsson, E., Arnthorsson, A.O., Helgason, D., Bjarnadottir, K., Ingvarsson, R.F., *et al.* (2020). Humoral Immune Response to SARS-CoV-2 in Iceland. N Engl J Med *383*, 1724-1734.

Gupta, A., Madhavan, M.V., Sehgal, K., Nair, N., Mahajan, S., Sehrawat, T.S., Bikdeli, B., Ahluwalia, N., Ausiello, J.C., Wan, E.Y., *et al.* (2020). Extrapulmonary manifestations of COVID-19. Nat Med *26*, 1017-1032.

Hemmat, N., Asadzadeh, Z., Ahangar, N.K., Alemohammad, H., Najafzadeh, B., Derakhshani, A., Baghbanzadeh, A., Baghi, H.B., Javadrashid, D., Najafi, S., *et al.* (2021). The roles of signaling pathways in SARS-CoV-2 infection; lessons learned from SARS-CoV and MERS-CoV. Archives of Virology *166*, 675-696.

Herrmann, J., Mori, V., Bates, J.H.T., and Suki, B. (2020). Modeling lung perfusion abnormalities to explain early COVID-19 hypoxemia. Nat Commun *11*, 4883.

Ho, W.Z., and Douglas, S.D. (1992). Glutathione and N-acetylcysteine suppression of human immunodeficiency virus replication in human monocyte/macrophages in vitro. AIDS Res Hum Retroviruses *8*, 1249-1253.

Hou, X., Liang, Y., Chen, J., Wei, Y., Zeng, P., Wang, L., Lu, C., and Diao, H. (2017). Expression Profiling of Cellular MicroRNA in Asymptomatic HBsAg Carriers and Chronic Hepatitis B Patients. Biomed Res Int *2017*, 6484835.

Hou, Z., Fan, F., and Liu, P. (2019). BTXA regulates the epithelial-mesenchymal transition and autophagy of keloid fibroblasts via modulating miR-1587/miR-2392 targeted ZEB2. Biosci Rep *39*.

Hu, H.M., Chen, Y., Liu, L., Zhang, C.G., Wang, W., Gong, K., Huang, Z., Guo, M.X., Li, W.X., and Li, W. (2013). C1orf61 acts as a tumor activator in human hepatocellular carcinoma and is associated with tumorigenesis and metastasis. FASEB J *27*, 163-173.

Hu, S., Li, Z., Lan, Y., Guan, J., Zhao, K., Chu, D., Fan, G., Guo, Y., Gao, F., and He, W. (2020). MiR-10a-5p-Mediated Syndecan 1 Suppression Restricts Porcine Hemagglutinating Encephalomyelitis Virus Replication. Front Microbiol *11*, 105.

Huang, C., Wang, Y., Li, X., Ren, L., Zhao, J., Hu, Y., Zhang, L., Fan, G., Xu, J., Gu, X., *et al.* (2020). Clinical features of patients infected with 2019 novel coronavirus in Wuhan, China. Lancet *395*, 497-506.

Hultstrom, M., Lipcsey, M., Wallin, E., Larsson, I.M., Larsson, A., and Frithiof, R. (2021). Severe acute kidney injury associated with progression of chronic kidney disease after critical COVID-19. Crit Care *25*, 37.

Ibrahim, H., Perl, A., Smith, D., Lewis, T., Kon, Z., Goldenberg, R., Yarta, K., Staniloae, C., and Williams, M. (2020). Therapeutic blockade of inflammation in severe COVID-19 infection with intravenous N-acetylcysteine. Clin Immunol *219*, 108544.

Islam, M.S., and Islam, A.B.M.M.K. (2021). Viral miRNAs confer survival in host cells by targeting apoptosis related host genes. Informatics in Medicine Unlocked *22*, 100501.

Jacobs, L.G., Gourna Paleoudis, E., Lesky-Di Bari, D., Nyirenda, T., Friedman, T., Gupta, A., Rasouli, L., Zetkulic, M., Balani, B., Ogedegbe, C., *et al.* (2020). Persistence of symptoms and quality of life at 35 days after hospitalization for COVID-19 infection. PLoS One *15*, e0243882.

Janssen, H.L., Reesink, H.W., Lawitz, E.J., Zeuzem, S., Rodriguez-Torres, M., Patel, K., van der Meer, A.J., Patick, A.K., Chen, A., Zhou, Y., *et al.* (2013). Treatment of HCV infection by targeting microRNA. N Engl J Med *368*, 1685-1694.

Jia, D., Koonce, N.A., Griffin, R.J., Jackson, C., and Corry, P.M. (2010). Prevention and mitigation of acute death of mice after abdominal irradiation by the antioxidant N-acetyl-cysteine (NAC). Radiat Res *173*, 579-589.

Jiang, Q., Wang, Y., Hao, Y., Juan, L., Teng, M., Zhang, X., Li, M., Wang, G., and Liu, Y. (2009). miR2Disease: a manually curated database for microRNA deregulation in human disease. Nucleic Acids Res *37*, D98-104.

Jima, D.D., Zhang, J., Jacobs, C., Richards, K.L., Dunphy, C.H., Choi, W.W., Au, W.Y., Srivastava, G., Czader, M.B., Rizzieri, D.A., *et al.* (2010). Deep sequencing of the small RNA transcriptome of normal and malignant human B cells identifies hundreds of novel microRNAs. Blood *116*, e118-127.

Johansen, M.D., Irving, A., Montagutelli, X., Tate, M.D., Rudloff, I., Nold, M.F., Hansbro, N.G., Kim, R.Y., Donovan, C., Liu, G., *et al.* (2020). Animal and translational models of SARS-CoV-2 infection and COVID-19. Mucosal Immunol *13*, 877-891.

Jopling, C.L., Yi, M., Lancaster, A.M., Lemon, S.M., and Sarnow, P. (2005). Modulation of hepatitis C virus RNA abundance by a liver-specific MicroRNA. Science *309*, 1577-1581.

1451 Kent, W.J., Sugnet, C.W., Furey, T.S., Roskin, K.M., Pringle, T.H., Zahler, A.M., and Haussler,
1452 D. (2002). The human genome browser at UCSC. Genome Res *12*, 996-1006.

1453 Kharazmi, A., Nielsen, H., and Schiotz, P.O. (1988). N-acetylcysteine inhibits human neutrophil
1454 and monocyte chemotaxis and oxidative metabolism. Int J Immunopharmacol *10*, 39-46.

1455 Kolde, R. (2015). pheatmap: Pretty heatmaps [Software].

1456 Korotkevich, G., Sukhov, V., Budin, N., Shpak, B., Artyomov, M.N., and Sergushichev, A.
1457 (2021). Fast gene set enrichment analysis. bioRxiv, 060012.

1458 Koumpa, F.S., Forde, C.T., and Manjaly, J.G. (2020). Sudden irreversible hearing loss post
1459 COVID-19. BMJ Case Rep *13*.

1460 Kovaka, S., Zimin, A.V., Pertea, G.M., Razaghi, R., Salzberg, S.L., and Pertea, M. (2019).
1461 Transcriptome assembly from long-read RNA-seq alignments with StringTie2. Genome Biol *20*,
1462 278.

1463 Kozomara, A., Birgaoanu, M., and Griffiths-Jones, S. (2019). miRBase: from microRNA
1464 sequences to function. Nucleic Acids Res *47*, D155-D162.

1465 Krajewski, P.K., Maj, J., and Szepietowski, J.C. (2021). Cutaneous Hyperaesthesia in SARS-
1466 CoV-2 Infection: Rare but not Unique Clinical Manifestation. Acta Derm Venereol *101*,
1467 adv00366.

1468 Lamb, J., Crawford, E.D., Peck, D., Modell, J.W., Blat, I.C., Wrobel, M.J., Lerner, J., Brunet,
1469 J.P., Subramanian, A., Ross, K.N., *et al.* (2006). The Connectivity Map: using gene-expression
1470 signatures to connect small molecules, genes, and disease. Science *313*, 1929-1935.

1471 Lawrie, C.H., Gal, S., Dunlop, H.M., Pushkaran, B., Liggins, A.P., Pulford, K., Banham, A.H.,
1472 Pezzella, F., Boultwood, J., Wainscoat, J.S., *et al.* (2008). Detection of elevated levels of tumour-
1473 associated microRNAs in serum of patients with diffuse large B-cell lymphoma. Br J Haematol
1474 *141*, 672-675.

1475 Ledford, H. (2020). Coronavirus breakthrough: dexamethasone is first drug shown to save lives.
1476 Nature *582*, 469.

1477 Li, J., Li, T., Lu, Y., Shen, G., Guo, H., Wu, J., Lei, C., Du, F., Zhou, F., Zhao, X., *et al.* (2017).
1478 MiR-2392 suppresses metastasis and epithelial-mesenchymal transition by targeting MAML3
1479 and WHSC1 in gastric cancer. FASEB J *31*, 3774-3786.

1480 Li, K., Chen, G., Hou, H., Liao, Q., Chen, J., Bai, H., Lee, S., Wang, C., Li, H., Cheng, L., *et al.*
1481 (2021). Analysis of sex hormones and menstruation in COVID-19 women of child-bearing age.
1482 Reprod Biomed Online *42*, 260-267.

1483 Liu, X., Wang, S., Meng, F., Wang, J., Zhang, Y., Dai, E., Yu, X., Li, X., and Jiang, W. (2013).
1484 SM2miR: a database of the experimentally validated small molecules' effects on microRNA
1485 expression. Bioinformatics *29*, 409-411.

1486 Lott, M.T., Leipzig, J.N., Derbeneva, O., Xie, H.M., Chalkia, D., Sarmady, M., Procaccio, V.,
1487 and Wallace, D.C. (2013). mtDNA Variation and Analysis Using Mitomap and Mitomaster. Curr
1488 Protoc Bioinformatics *44*, 1 23 21-26.

1489 Love, M.I., Huber, W., and Anders, S. (2014). Moderated estimation of fold change and
1490 dispersion for RNA-seq data with DESeq2. Genome Biol *15*, 550.

1491 Loza, M.J., McCall, C.E., Li, L., Isaacs, W.B., Xu, J., and Chang, B.L. (2007). Assembly of
1492 inflammation-related genes for pathway-focused genetic analysis. PLoS One *2*, e1035.

1493 Ma, Y., Wang, C., Xue, M., Fu, F., Zhang, X., Li, L., Yin, L., Xu, W., Feng, L., and Liu, P.
1494 (2018). The Coronavirus Transmissible Gastroenteritis Virus Evades the Type I Interferon
1495 Response through IRE1alpha-Mediated Manipulation of the MicroRNA miR-30a-5p/SOCS1/3
1496 Axis. J Virol *92*.

1497 Mahajan, A., and Mason, G.F. (2021). A sobering addition to the literature on COVID-19 and
1498 the brain. J Clin Invest.

1499 Malik, Z.R., Razaq, Z., Siff, M., and Sheikh, S. (2020). COVID-19 Presenting as Banti's
1500 Syndrome. Cureus *12*, e9096.

1501 Mishra, P.K., Tandon, R., and Byrareddy, S.N. (2020). Diabetes and COVID-19 risk: an miRNA
1502 perspective. Am J Physiol Heart Circ Physiol *319*, H604-H609.

1503 Mitchell, P.S., Parkin, R.K., Kroh, E.M., Fritz, B.R., Wyman, S.K., Pogosova-Agadjanyan, E.L.,
1504 Peterson, A., Noteboom, J., O'Briant, K.C., Allen, A., *et al.* (2008). Circulating microRNAs as
1505 stable blood-based markers for cancer detection. Proc Natl Acad Sci U S A *105*, 10513-10518.

1506 Nagy, A., Lanczky, A., Menyhart, O., and Gyorffy, B. (2018). Validation of miRNA prognostic
1507 power in hepatocellular carcinoma using expression data of independent datasets. Sci Rep *8*,
1508 9227.

1509 Nagy, A., Munkacsy, G., and Gyorffy, B. (2021). Pancancer survival analysis of cancer hallmark
1510 genes. Sci Rep *11*, 6047.

1511 Nersisyan, S., Engibaryan, N., Gorbonos, A., Kirdey, K., Makhonin, A., and Tonevitsky, A.
1512 (2020). Potential role of cellular miRNAs in coronavirus-host interplay. PeerJ *8*, e9994.

1513 Nishiga, M., Wang, D.W., Han, Y., Lewis, D.B., and Wu, J.C. (2020). COVID-19 and
1514 cardiovascular disease: from basic mechanisms to clinical perspectives. Nat Rev Cardiol *17*, 543-
1515 558.

1516 Ochsner, S.A., Pillich, R.T., and McKenna, N.J. (2020). Consensus transcriptional regulatory
1517 networks of coronavirus-infected human cells. Sci Data *7*, 314.

1518 Ottosen, S., Parsley, T.B., Yang, L., Zeh, K., van Doorn, L.J., van der Veer, E., Raney, A.K.,
1519 Hodges, M.R., and Patick, A.K. (2015). In vitro antiviral activity and preclinical and clinical
1520 resistance profile of miravirsen, a novel anti-hepatitis C virus therapeutic targeting the human
1521 factor miR-122. Antimicrob Agents Chemother *59*, 599-608.

1522 Park, J., Foox, J., Hether, T., Danko, D., Warren, S., Kim, Y., Reeves, J., Butler, D.J., Mozsary,
1523 C., Rosiene, J., *et al.* (2021). Systemic Tissue and Cellular Disruption from SARS-CoV-2
1524 Infection revealed in COVID-19 Autopsies and Spatial Omics Tissue Maps. bioRxiv,
1525 2021.2003.2008.434433.

1526 Park, J.L., Park, S.M., Kwon, O.H., Lee, H.C., Kim, J.Y., Seok, H.H., Lee, W.S., Lee, S.H.,
1527 Kim, Y.S., Woo, K.M., *et al.* (2014). Microarray screening and qRT-PCR evaluation of
1528 microRNA markers for forensic body fluid identification. Electrophoresis *35*, 3062-3068.

1529 Patro, R., Duggal, G., Love, M.I., Irizarry, R.A., and Kingsford, C. (2017). Salmon provides fast
1530 and bias-aware quantification of transcript expression. Nat Methods *14*, 417-419.

Polack, F.P., Thomas, S.J., Kitchin, N., Absalon, J., Gurtman, A., Lockhart, S., Perez, J.L., Perez Marc, G., Moreira, E.D., Zerbini, C., *et al.* (2020). Safety and Efficacy of the BNT162b2 mRNA Covid-19 Vaccine. N Engl J Med *383*, 2603-2615.

Pontecorvi, G., Bellenghi, M., Ortona, E., and Care, A. (2020). microRNAs as new possible actors in gender disparities of Covid-19 pandemic. Acta Physiol (Oxf) *230*, e13538.

Poppe, M., Wittig, S., Jurida, L., Bartkuhn, M., Wilhelm, J., Muller, H., Beuerlein, K., Karl, N., Bhuju, S., Ziebuhr, J., *et al.* (2017). The NF-kappaB-dependent and -independent transcriptome and chromatin landscapes of human coronavirus 229E-infected cells. PLoS Pathog *13*, e1006286.

Portincasa, P., Krawczyk, M., Machill, A., Lammert, F., and Di Ciaula, A. (2020). Hepatic consequences of COVID-19 infection. Lapping or biting? Eur J Intern Med *77*, 18-24.

Rath, S., Sharma, R., Gupta, R., Ast, T., Chan, C., Durham, T.J., Goodman, R.P., Grabarek, Z., Haas, M.E., Hung, W.H.W., *et al.* (2021). MitoCarta3.0: an updated mitochondrial proteome now with sub-organelle localization and pathway annotations. Nucleic Acids Res *49*, D1541-D1547.

Rodriguez, M., Soler, Y., Perry, M., Reynolds, J.L., and El-Hage, N. (2020). Impact of Severe Acute Respiratory Syndrome Coronavirus 2 (SARS-CoV-2) in the Nervous System: Implications of COVID-19 in Neurodegeneration. Front Neurol *11*, 583459.

Rossi, R., Talarico, M., Coppi, F., and Boriani, G. (2020). Protective role of statins in COVID 19 patients: importance of pharmacokinetic characteristics rather than intensity of action. Intern Emerg Med *15*, 1573-1576.

Rother, N., Yanginlar, C., Lindeboom, R.G.H., Bekkering, S., van Leent, M.M.T., Buijsers, B., Jonkman, I., de Graaf, M., Baltissen, M., Lamers, L.A., *et al.* (2020). Hydroxychloroquine Inhibits the Trained Innate Immune Response to Interferons. Cell Rep Med *1*, 100146.

Rupaimoole, R., and Slack, F.J. (2017). MicroRNA therapeutics: towards a new era for the management of cancer and other diseases. Nat Rev Drug Discov *16*, 203-222.

Sacar Demirci, M.D., and Adan, A. (2020). Computational analysis of microRNA-mediated interactions in SARS-CoV-2 infection. PeerJ *8*, e9369.

Sadoff, J., Le Gars, M., Shukarev, G., Heerwegh, D., Truyers, C., de Groot, A.M., Stoop, J., Tete, S., Van Damme, W., Leroux-Roels, I., *et al.* (2021). Interim Results of a Phase 1-2a Trial of Ad26.COV2.S Covid-19 Vaccine. N Engl J Med.

Sadowska, A.M., Manuel-y-Keenoy, B., Vertongen, T., Schippers, G., Radomska-Lesniewska, D., Heytens, E., and De Backer, W.A. (2006). Effect of N-acetylcysteine on neutrophil activation markers in healthy volunteers: in vivo and in vitro study. Pharmacol Res *53*, 216-225.

Sardar, R., Satish, D., and Gupta, D. (2020). Identification of Novel SARS-CoV-2 Drug Targets by Host MicroRNAs and Transcription Factors Co-regulatory Interaction Network Analysis. Front Genet *11*, 571274.

Schult, P., Roth, H., Adams, R.L., Mas, C., Imbert, L., Orlik, C., Ruggieri, A., Pyle, A.M., and Lohmann, V. (2018). microRNA-122 amplifies hepatitis C virus translation by shaping the structure of the internal ribosomal entry site. Nat Commun *9*, 2613.

Self, W.H., Tenforde, M.W., Stubblefield, W.B., Feldstein, L.R., Steingrub, J.S., Shapiro, N.I., Ginde, A.A., Prekker, M.E., Brown, S.M., Peltan, I.D., *et al.* (2020). Decline in SARS-CoV-2 Antibodies After Mild Infection Among Frontline Health Care Personnel in a Multistate Hospital Network - 12 States, April-August 2020. MMWR Morb Mortal Wkly Rep *69*, 1762-1766.

Shannon, P., Markiel, A., Ozier, O., Baliga, N.S., Wang, J.T., Ramage, D., Amin, N., Schwikowski, B., and Ideker, T. (2003). Cytoscape: a software environment for integrated models of biomolecular interaction networks. Genome Res *13*, 2498-2504.

Shu, Y., and McCauley, J. (2017). GISAID: Global initiative on sharing all influenza data - from vision to reality. Euro Surveill *22*.

Singh, U., Hur, M., Dorman, K., and Wurtele, E.S. (2020). MetaOmGraph: a workbench for interactive exploratory data analysis of large expression datasets. Nucleic Acids Res *48*, e23.

Singh, U., Li, J., Seetharam, A., and Wurtele, E.S. (2021). pyrpipe: a python package for RNA-Seq workflows. bioRxiv, 2020.2003.2004.925818.

Sirin, D.A., and Ozcelik, F. (2021). The relationship between COVID-19 and the dental damage stage determined by radiological examination. Oral Radiol.

Sirota, M., Dudley, J.T., Kim, J., Chiang, A.P., Morgan, A.A., Sweet-Cordero, A., Sage, J., and Butte, A.J. (2011). Discovery and preclinical validation of drug indications using compendia of public gene expression data. Sci Transl Med *3*, 96ra77.

Srivastava, A., Malik, L., Sarkar, H., Zakeri, M., Almodaresi, F., Soneson, C., Love, M.I., Kingsford, C., and Patro, R. (2020). Alignment and mapping methodology influence transcript abundance estimation. Genome Biol *21*, 239.

Su, M., Chen, Y., Qi, S., Shi, D., Feng, L., and Sun, D. (2020). A Mini-Review on Cell Cycle Regulation of Coronavirus Infection. Front Vet Sci *7*, 586826.

Subramanian, A., Tamayo, P., Mootha, V.K., Mukherjee, S., Ebert, B.L., Gillette, M.A., Paulovich, A., Pomeroy, S.L., Golub, T.R., Lander, E.S., *et al.* (2005). Gene set enrichment analysis: a knowledge-based approach for interpreting genome-wide expression profiles. Proc Natl Acad Sci U S A *102*, 15545-15550.

Sullivan, K.D., Galbraith, M.D., Kinning, K.T., Bartsch, K., Levinsky, N., Araya, P., Smith, K.P., Granrath, R.E., Shaw, J.R., Baxter, R., *et al.* (2021). The COVIDome Explorer Researcher Portal. medRxiv.

Tang, H., Gao, Y., Li, Z., Miao, Y., Huang, Z., Liu, X., Xie, L., Li, H., Wen, W., Zheng, Y., *et al.* (2020). The noncoding and coding transcriptional landscape of the peripheral immune response in patients with COVID-19. Clin Transl Med *10*, e200.

Teodori, L., Sestili, P., Madiai, V., Coppari, S., Fraternale, D., Rocchi, M.B.L., Ramakrishna, S., and Albertini, M.C. (2020). MicroRNAs Bioinformatics Analyses Identifying HDAC Pathway as a Putative Target for Existing Anti-COVID-19 Therapeutics. Front Pharmacol *11*, 582003.

Thibault, P.A., Huys, A., Amador-Canizares, Y., Gailius, J.E., Pinel, D.E., and Wilson, J.A. (2015). Regulation of Hepatitis C Virus Genome Replication by Xrn1 and MicroRNA-122 Binding to Individual Sites in the 5' Untranslated Region. J Virol *89*, 6294-6311.

Tribolet, L., Kerr, E., Cowled, C., Bean, A.G.D., Stewart, C.R., Dearnley, M., and Farr, R.J. (2020). MicroRNA Biomarkers for Infectious Diseases: From Basic Research to Biosensing. Front Microbiol *11*, 1197.

Trobaugh, D.W., and Klimstra, W.B. (2017). MicroRNA Regulation of RNA Virus Replication and Pathogenesis. Trends Mol Med *23*, 80-93.

V'Kovski, P., Kratzel, A., Steiner, S., Stalder, H., and Thiel, V. (2021). Coronavirus biology and replication: implications for SARS-CoV-2. Nat Rev Microbiol *19*, 155-170.

van der Ree, M.H., de Vree, J.M., Stelma, F., Willemse, S., van der Valk, M., Rietdijk, S., Molenkamp, R., Schinkel, J., van Nuenen, A.C., Beuers, U., *et al.* (2017). Safety, tolerability, and antiviral effect of RG-101 in patients with chronic hepatitis C: a phase 1B, double-blind, randomised controlled trial. Lancet *389*, 709-717.

Vejnar, C.E., and Zdobnov, E.M. (2012). MiRmap: comprehensive prediction of microRNA target repression strength. Nucleic Acids Res *40*, 11673-11683.

Wallace, D.C. (2018). Mitochondrial genetic medicine. Nat Genet *50*, 1642-1649.

Walsh-Messinger, J., Manis, H., Vrabec, A., Sizemore, J., Bishof, K., Debidda, M., Malaspina, D., and Greenspan, N. (2020). The Kids Are Not Alright: A Preliminary Report of Post-COVID Syndrome in University Students. medRxiv.

West, A.P., Khoury-Hanold, W., Staron, M., Tal, M.C., Pineda, C.M., Lang, S.M., Bestwick, M., Duguay, B.A., Raimundo, N., MacDuff, D.A., *et al.* (2015). Mitochondrial DNA stress primes the antiviral innate immune response. Nature *520*, 553-557.

West, A.P., and Shadel, G.S. (2017). Mitochondrial DNA in innate immune responses and inflammatory pathology. Nat Rev Immunol *17*, 363-375.

Wickham, H. (2016). ggplot2: Elegant Graphics for Data Analysis (Springer-Verlag New York).

Widiasta, A., Sribudiani, Y., Nugrahapraja, H., Hilmanto, D., Sekarwana, N., and Rachmadi, D. (2020). Potential role of ACE2-related microRNAs in COVID-19-associated nephropathy. Noncoding RNA Res *5*, 153-166.

Yang, J., Li, C., Li, H., and E, C. (2019). LncRNA CACNA1G-AS1 facilitates hepatocellular carcinoma progression through the miR-2392/C1orf61 pathway. J Cell Physiol *234*, 18415-18422.

Yang, S., Pei, Y., Li, X., Zhao, S., Zhu, M., and Zhao, A. (2016). miR-124 attenuates Japanese encephalitis virus replication by targeting DNM2. Virol J *13*, 105.

Younis, J.S., Abassi, Z., and Skorecki, K. (2020). Is there an impact of the COVID-19 pandemic on male fertility? The ACE2 connection. Am J Physiol Endocrinol Metab *318*, E878-E880.

Zamani, B., Moeini Taba, S.M., and Shayestehpour, M. (2021). Systemic lupus erythematosus manifestation following COVID-19: a case report. J Med Case Rep *15*, 29.

Zhong, Z., Liang, S., Sanchez-Lopez, E., He, F., Shalapour, S., Lin, X.J., Wong, J., Ding, S., Seki, E., Schnabl, B., *et al.* (2018). New mitochondrial DNA synthesis enables NLRP3 inflammasome activation. Nature *560*, 198-203.

Zhu, N., Zhang, D., Wang, W., Li, X., Yang, B., Song, J., Zhao, X., Huang, B., Shi, W., Lu, R., *et al.* (2020). A Novel Coronavirus from Patients with Pneumonia in China, 2019. N Engl J Med *382*, 727-733.

Abdelrahman, Z., Liu, Q., Jiang, S., Li, M., Sun, Q., Zhang, Y., and Wang, X. (2021). Evaluation of the Current Therapeutic Approaches for COVID-19: A Systematic Review and a Meta-analysis. Front Pharmacol *12*, 607408.

Alamdari, D.H., Moghaddam, A.B., Amini, S., Keramati, M.R., Zarmehri, A.M., Alamdari, A.H., Damsaz, M., Banpour, H., Yarahmadi, A., and Koliakos, G. (2020). Application of methylene blue -vitamin C -N-acetyl cysteine for treatment of critically ill COVID-19 patients, report of a phase-I clinical trial. Eur J Pharmacol *885*, 173494.

Ardestani, A., and Azizi, Z. (2021). Targeting glucose metabolism for treatment of COVID-19. Signal Transduct Target Ther *6*, 112.

Bojkova, D., Klann, K., Koch, B., Widera, M., Krause, D., Ciesek, S., Cinatl, J., and Munch, C. (2020). Proteomics of SARS-CoV-2-infected host cells reveals therapy targets. Nature *583*, 469-472.

Codo, A.C., Davanzo, G.G., Monteiro, L.B., de Souza, G.F., Muraro, S.P., Virgilio-da-Silva, J.V., Prodonoff, J.S., Carregari, V.C., de Biagi Junior, C.A.O., Crunfli, F., *et al.* (2020). Elevated Glucose Levels Favor SARS-CoV-2 Infection and Monocyte Response through a HIF-1alpha/Glycolysis-Dependent Axis. Cell Metab *32*, 437-446 e435.

Mishra, P.K., Tandon, R., and Byrareddy, S.N. (2020). Diabetes and COVID-19 risk: an miRNA perspective. Am J Physiol Heart Circ Physiol *319*, H604-H609.

Nersisyan, S., Engibaryan, N., Gorbonos, A., Kirdey, K., Makhonin, A., and Tonevitsky, A. (2020). Potential role of cellular miRNAs in coronavirus-host interplay. PeerJ *8*, e9994.

Overbey, E.G., Saravia-Butler, A.M., Zhang, Z., Rathi, K.S., Fogle, H., da Silveira, W.A., Barker, R.J., Bass, J.J., Beheshti, A., Berrios, D.C., *et al.* (2021). NASA GeneLab RNA-seq consensus pipeline: standardized processing of short-read RNA-seq data. iScience *24*.

Portincasa, P., Krawczyk, M., Machill, A., Lammert, F., and Di Ciaula, A. (2020). Hepatic consequences of COVID-19 infection. Lapping or biting? Eur J Intern Med *77*, 18-24.

Ren, L., Zhang, R., Rao, J., Xiao, Y., Zhang, Z., Yang, B., Cao, D., Zhong, H., Ning, P., Shang, Y., *et al.* (2018). Transcriptionally Active Lung Microbiome and Its Association with Bacterial Biomass and Host Inflammatory Status. mSystems *3*.

Ritchie, M.E., Phipson, B., Wu, D., Hu, Y., Law, C.W., Shi, W., and Smyth, G.K. (2015). limma powers differential expression analyses for RNA-sequencing and microarray studies. Nucleic Acids Res *43*, e47.

Sacar Demirci, M.D., and Adan, A. (2020). Computational analysis of microRNA-mediated interactions in SARS-CoV-2 infection. PeerJ *8*, e9369.

Sardar, R., Satish, D., and Gupta, D. (2020). Identification of Novel SARS-CoV-2 Drug Targets by Host MicroRNAs and Transcription Factors Co-regulatory Interaction Network Analysis. Front Genet *11*, 571274.

Shen, Z., Xiao, Y., Kang, L., Ma, W., Shi, L., Zhang, L., Zhou, Z., Yang, J., Zhong, J., Yang, D., *et al.* (2020). Genomic Diversity of Severe Acute Respiratory Syndrome-Coronavirus 2 in Patients With Coronavirus Disease 2019. Clin Infect Dis *71*, 713-720.

1690 Stukalov, A., Girault, V., Grass, V., Karayel, O., Bergant, V., Urban, C., Haas, D.A., Huang, Y.,
1691 Oubraham, L., Wang, A., *et al.* (2021). Multilevel proteomics reveals host perturbations by
1692 SARS-CoV-2 and SARS-CoV. bioRxiv, 2020.2006.2017.156455.

1693 Teodori, L., Sestili, P., Madiai, V., Coppari, S., Fraternale, D., Rocchi, M.B.L., Ramakrishna, S.,
1694 and Albertini, M.C. (2020). MicroRNAs Bioinformatics Analyses Identifying HDAC Pathway as
1695 a Putative Target for Existing Anti-COVID-19 Therapeutics. Front Pharmacol *11*, 582003.

1696 Widiasta, A., Sribudiani, Y., Nugrahapraja, H., Hilmanto, D., Sekarwana, N., and Rachmadi, D.
1697 (2020). Potential role of ACE2-related microRNAs in COVID-19-associated nephropathy.
1698 Noncoding RNA Res *5*, 153-166.

1699 Zhang, S., Amahong, K., Sun, X., Lian, X., Liu, J., Sun, H., Lou, Y., Zhu, F., and Qiu, Y. (2021).
1700 The miRNA: a small but powerful RNA for COVID-19. Brief Bioinform *22*, 1137-1149.

1701

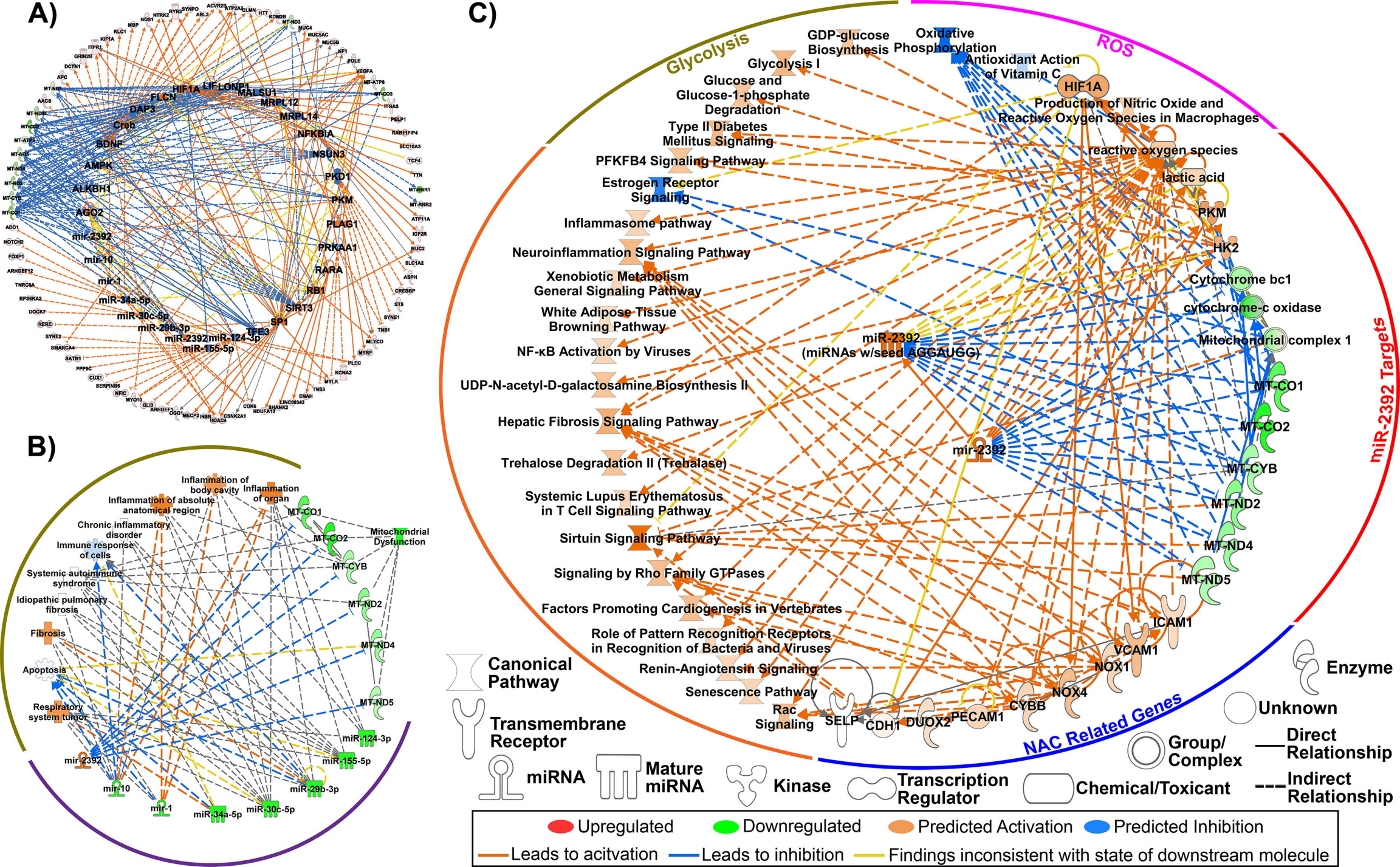
A)
HIF1A
LIF
LONP1
MALSU1
MRPL12
MRPL14
NFKBIA
NSUN3
PKD1
PKM
PLAG1
PRKAA1
RARA
RB1
SIRT3
SP1
TFE3
FLCN
DAP3
Creb
BDNF
AMPK
ALKBH1
AGO2
mir-2392
mir-10
mir-1
miR-34a-5p
miR-30c-5p
miR-29b-3p
miR-2392
miR-124-3p
miR-155-5p
B)
Inflammation of body cavity
Inflammation of organ
Inflammation of absolute anatomical region
Chronic inflammatory disorder
Immune response of cells
Systemic autoimmune syndrome
Idiopathic pulmonary fibrosis
Fibrosis
Apoptosis
Respiratory system tumor
MT-CO1
MT-CO2
MT-CYB
MT-ND2
MT-ND4
MT-ND5
Mitochondrial Dysfunction
mir-2392
mir-10
mir-1
miR-34a-5p
miR-30c-5p
miR-29b-3p
miR-155-5p
miR-124-3p
C)
Glycolysis
ROS
GDP-glucose Biosynthesis
Oxidative Phosphorylation
Glycolysis I
Antioxidant Action of Vitamin C
Glucose and Glucose-1-phosphate Degradation
HIF1A
Production of Nitric Oxide and Reactive Oxygen Species in Macrophages
Type II Diabetes Mellitus Signaling
reactive oxygen species
PFKFB4 Signaling Pathway
lactic acid
Estrogen Receptor Signaling
PKM
Inflammasome pathway
HK2
Neuroinflammation Signaling Pathway
Cytochrome bc1
Xenobiotic Metabolism General Signaling Pathway
cytochrome-c oxidase
White Adipose Tissue Browning Pathway
Mitochondrial complex 1
NF-κB Activation by Viruses
miR-2392 (miRNAs w/seed AGGAUGG)
MT-CO1
UDP-N-acetyl-D-galactosamine Biosynthesis II
MT-CO2
Hepatic Fibrosis Signaling Pathway
mir-2392
MT-CYB
Trehalose Degradation II (Trehalase)
MT-ND2
Systemic Lupus Erythematosus in T Cell Signaling Pathway
MT-ND4
Sirtuin Signaling Pathway
MT-ND5
Signaling by Rho Family GTPases
ICAM1
Factors Promoting Cardiogenesis in Vertebrates
VCAM1
Role of Pattern Recognition Receptors in Recognition of Bacteria and Viruses
NOX1
Renin-Angiotensin Signaling
NOX4
Senescence Pathway
CYBB
Rac Signaling
SELP
CDH1
DUOX2
PECAM1
miR-2392 Targets
NAC Related Genes
Canonical Pathway
Transmembrane Receptor
miRNA
Mature miRNA
Kinase
Transcription Regulator
Enzyme
Unknown
Group/ Complex
Chemical/Toxicant
Direct Relationship
Indirect Relationship
Upregulated
Downregulated
Predicted Activation
Predicted Inhibition
Leads to acitvation
Leads to inhibition
Findings inconsistent with state of downstream molecule

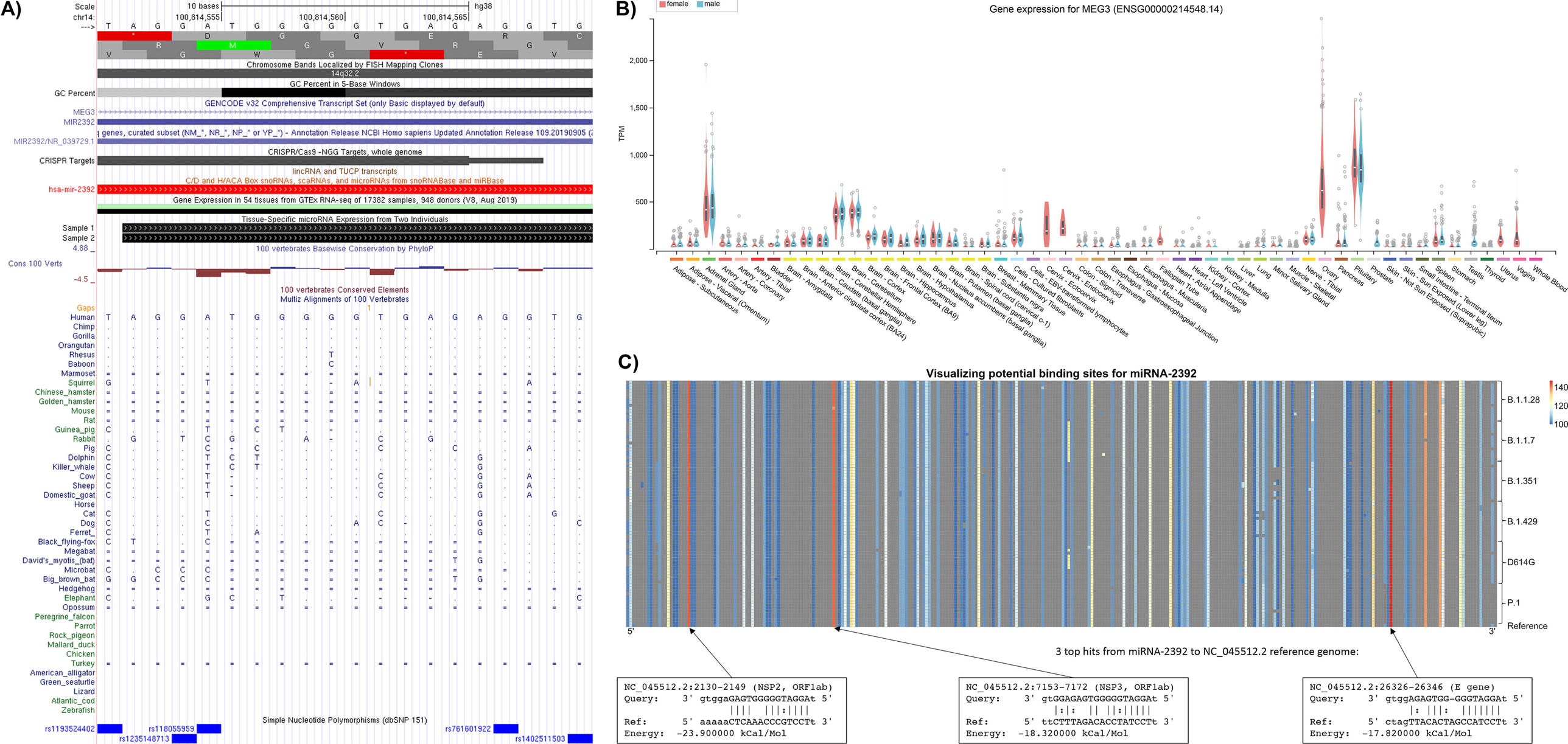
A)
Scale
chr14:
10 bases
hg38
100,814,555
100,814,560
100,814,565
Chromosome Bands Localized by FISH Mapping Clones
14q32.2
GC Percent in 5-Base Windows
GC Percent
GENCODE v32 Comprehensive Transcript Set (only Basic displayed by default)
MEG3
MIR2392
genes, curated subset (NM_*, NR_*, NP_* or YP_*) - Annotation Release NCBI Homo sapiens Updated Annotation Release 109.20190905
MIR2392/NR_039729.1
CRISPR/Cas9 -NGG Targets, whole genome
CRISPR Targets
lincRNA and TUCP transcripts
C/D and H/ACA Box snoRNAs, scaRNAs, and microRNAs from snoRNABase and miRBase
hsa-mir-2392
Gene Expression in 54 tissues from GTEx RNA-seq of 17382 samples, 948 donors (V8, Aug 2019)
Tissue-Specific microRNA Expression from Two Individuals
Sample 1
Sample 2
4.88
100 vertebrates Basewise Conservation by PhyloP
Cons 100 Verts
-4.5
100 vertebrates Conserved Elements
Multiz Alignments of 100 Vertebrates
Gaps
Human
Chimp
Gorilla
Orangutan
Rhesus
Baboon
Marmoset
Squirrel
Chinese_hamster
Golden_hamster
Mouse
Rat
Guinea_pig
Rabbit
Pig
Dolphin
Killer_whale
Cow
Sheep
Domestic_goat
Horse
Cat
Dog
Ferret
Black_flying-fox
Megabat
David's_myotis_(bat)
Microbat
Big_brown_bat
Hedgehog
Elephant
Opossum
Peregrine_falcon
Parrot
Rock_pigeon
Mallard_duck
Chicken
Turkey
American_alligator
Green_seaturtle
Lizard
Atlantic_cod
Zebrafish
Simple Nucleotide Polymorphisms (dbSNP 151)
rs1193524402
rs1235148713
rs118055959
rs761601922
rs1402511503
B)
female
male
Gene expression for MEG3 (ENSG00000214548.14)
TPM
2,000
1,500
1,000
500
Adipose - Subcutaneous
Adipose - Visceral (Omentum)
Adrenal Gland
Artery - Aorta
Artery - Coronary
Artery - Tibial
Bladder
Brain - Amygdala
Brain - Anterior cingulate cortex (BA24)
Brain - Caudate (basal ganglia)
Brain - Cerebellar Hemisphere
Brain - Cerebellum
Brain - Cortex
Brain - Frontal Cortex (BA9)
Brain - Hippocampus
Brain - Hypothalamus
Brain - Nucleus accumbens (basal ganglia)
Brain - Putamen (basal ganglia)
Brain - Spinal cord (cervical c-1)
Brain - Substantia nigra
Breast - Mammary Tissue
Cells - Cultured fibroblasts
Cells - EBV-transformed lymphocytes
Cervix - Ectocervix
Cervix - Endocervix
Colon - Sigmoid
Colon - Transverse
Esophagus - Gastroesophageal Junction
Esophagus - Mucosa
Esophagus - Muscularis
Fallopian Tube
Heart - Atrial Appendage
Heart - Left Ventricle
Kidney - Cortex
Kidney - Medulla
Liver
Lung
Minor Salivary Gland
Muscle - Skeletal
Nerve - Tibial
Ovary
Pancreas
Pituitary
Prostate
Skin - Not Sun Exposed (Suprapubic)
Skin - Sun Exposed (Lower leg)
Small Intestine - Terminal Ileum
Spleen
Stomach
Testis
Thyroid
Uterus
Vagina
Whole Blood
C)
Visualizing potential binding sites for miRNA-2392
140
120
100
B.1.1.28
B.1.1.7
B.1.351
B.1.429
D614G
P.1
Reference
5'
3'
3 top hits from miRNA-2392 to NC_045512.2 reference genome:
NC_045512.2:2130-2149 (NSP2, ORF1ab)
Query: 3' gtggaGAGTGGGGGTAGGAt 5'
|||| |||:||||
Ref: 5' aaaaaCTCAAACCCGTCCTt 3'
Energy: -23.900000 kCal/Mol
NC_045512.2:7153-7172 (NSP3, ORF1ab)
Query: 3' gtGGAGAGTGGGGGTAGGAt 5'
|:|: || ||:|||||
Ref: 5' ttCTTTAGACACCTATCCTt 3'
Energy: -18.320000 kCal/Mol
NC_045512.2:26326-26346 (E gene)
Query: 3' gtggAGAGTGG-GGGTAGGAt 5'
|: |||: |||||||
Ref: 5' ctagTTACACTAGCCATCCTt 3'
Energy: -17.820000 kCal/Mol

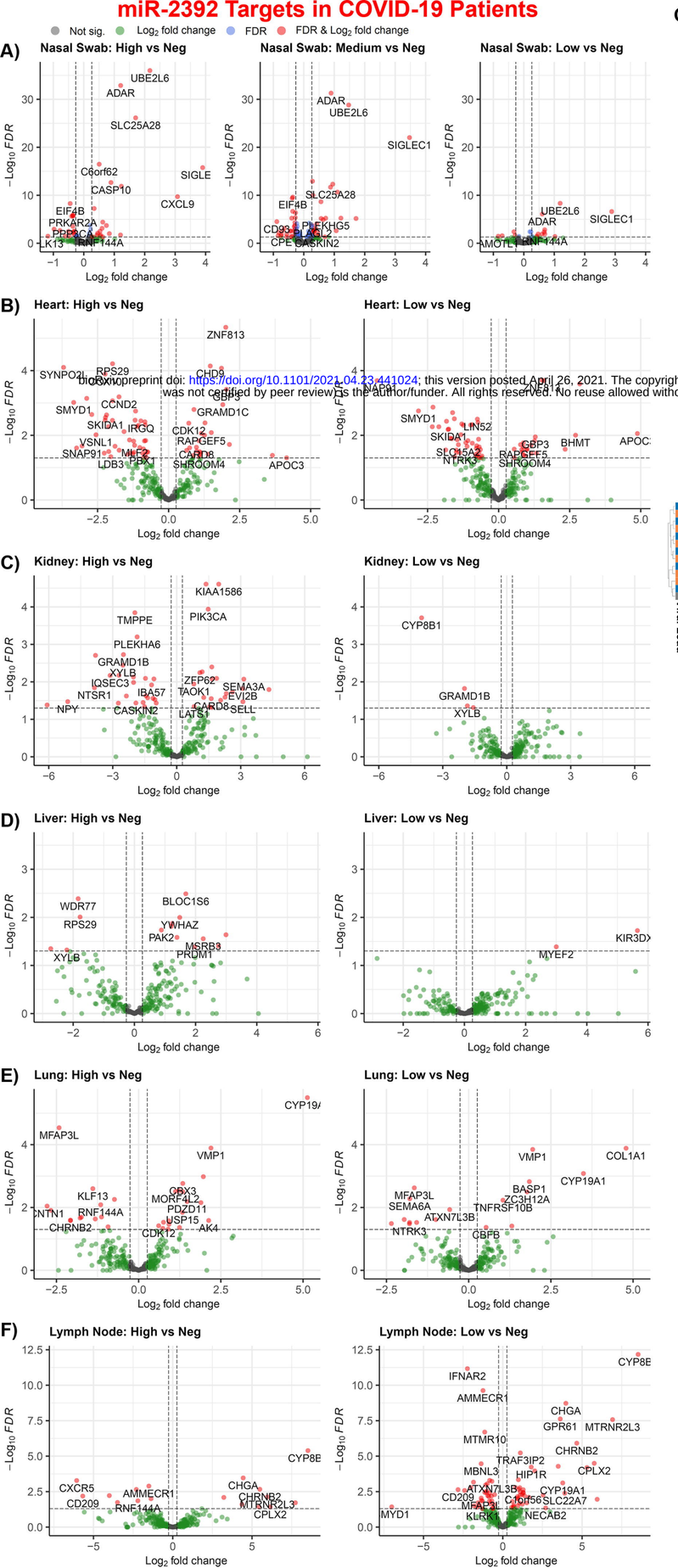

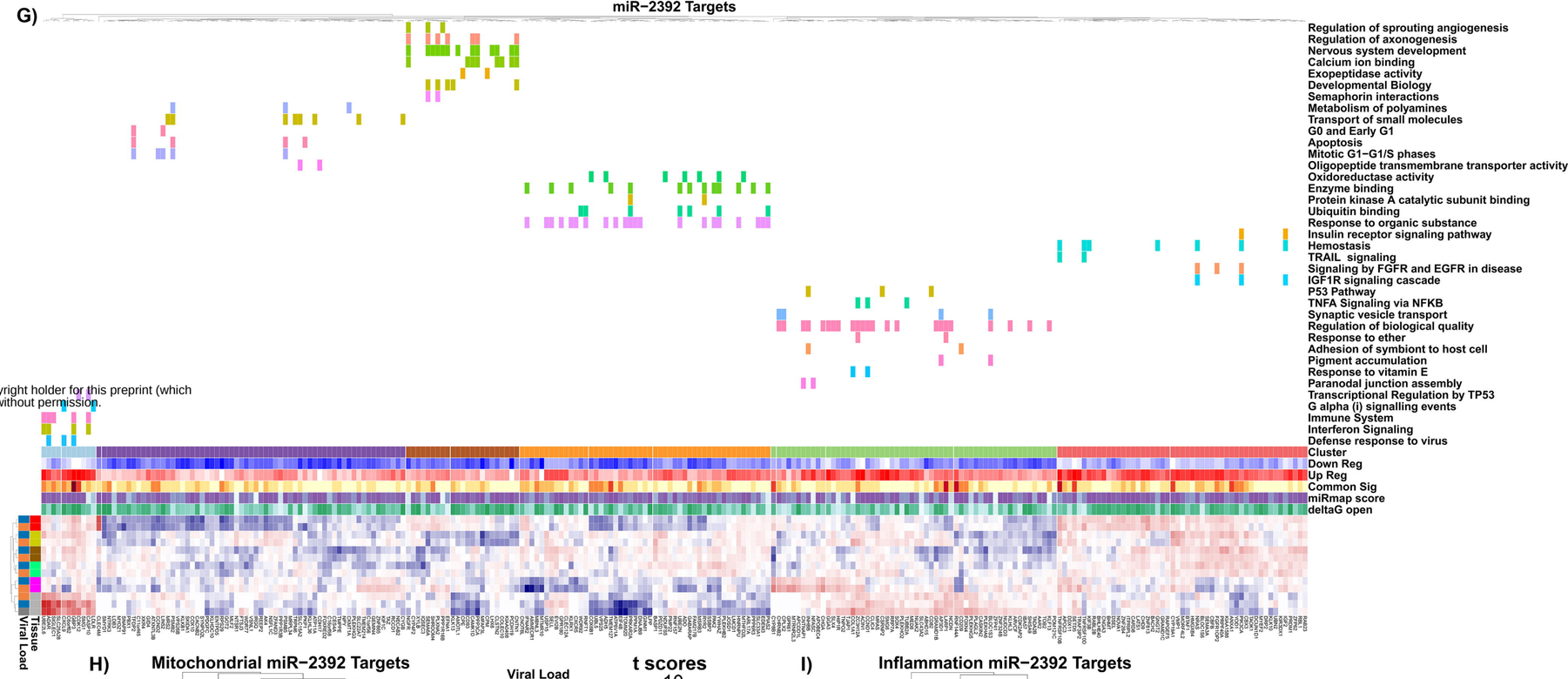

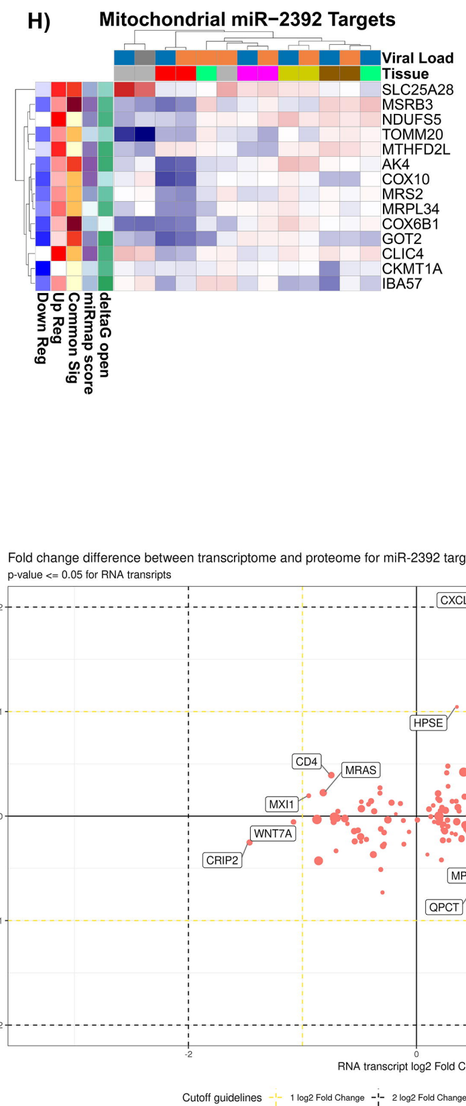

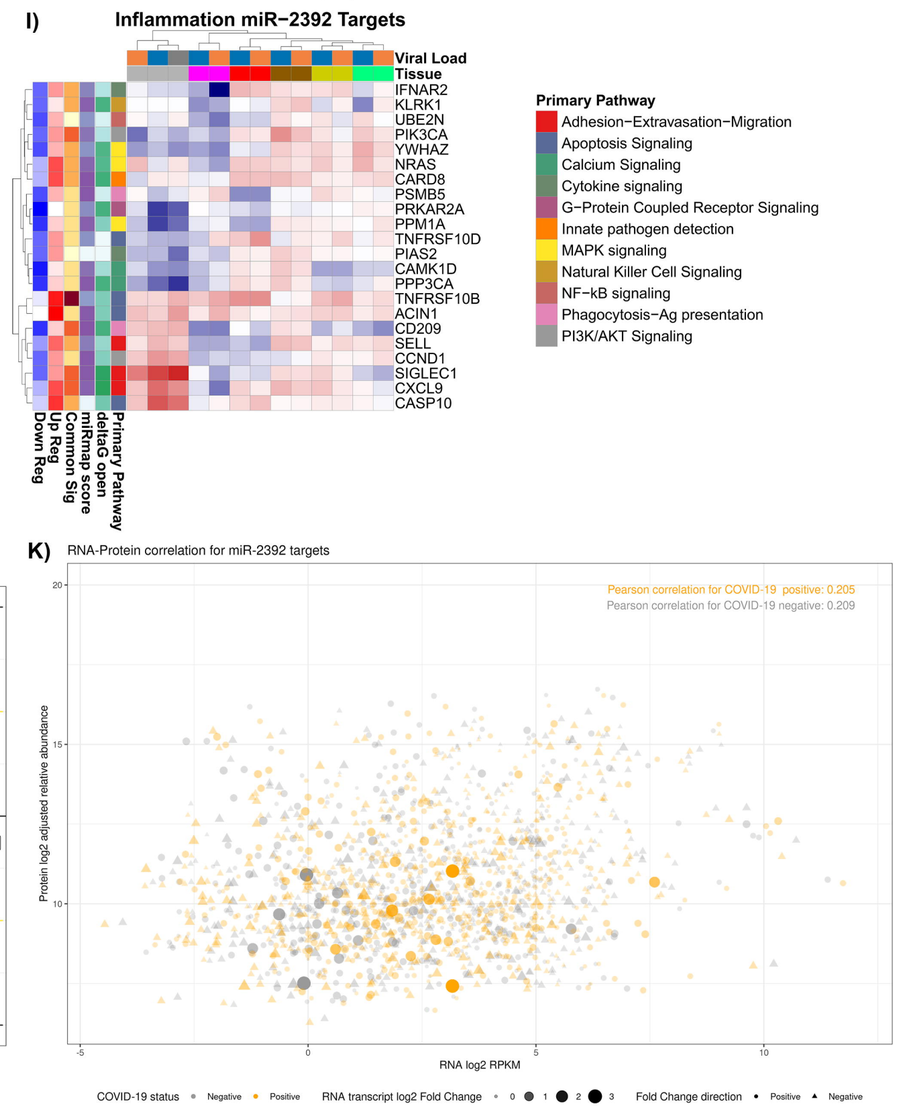

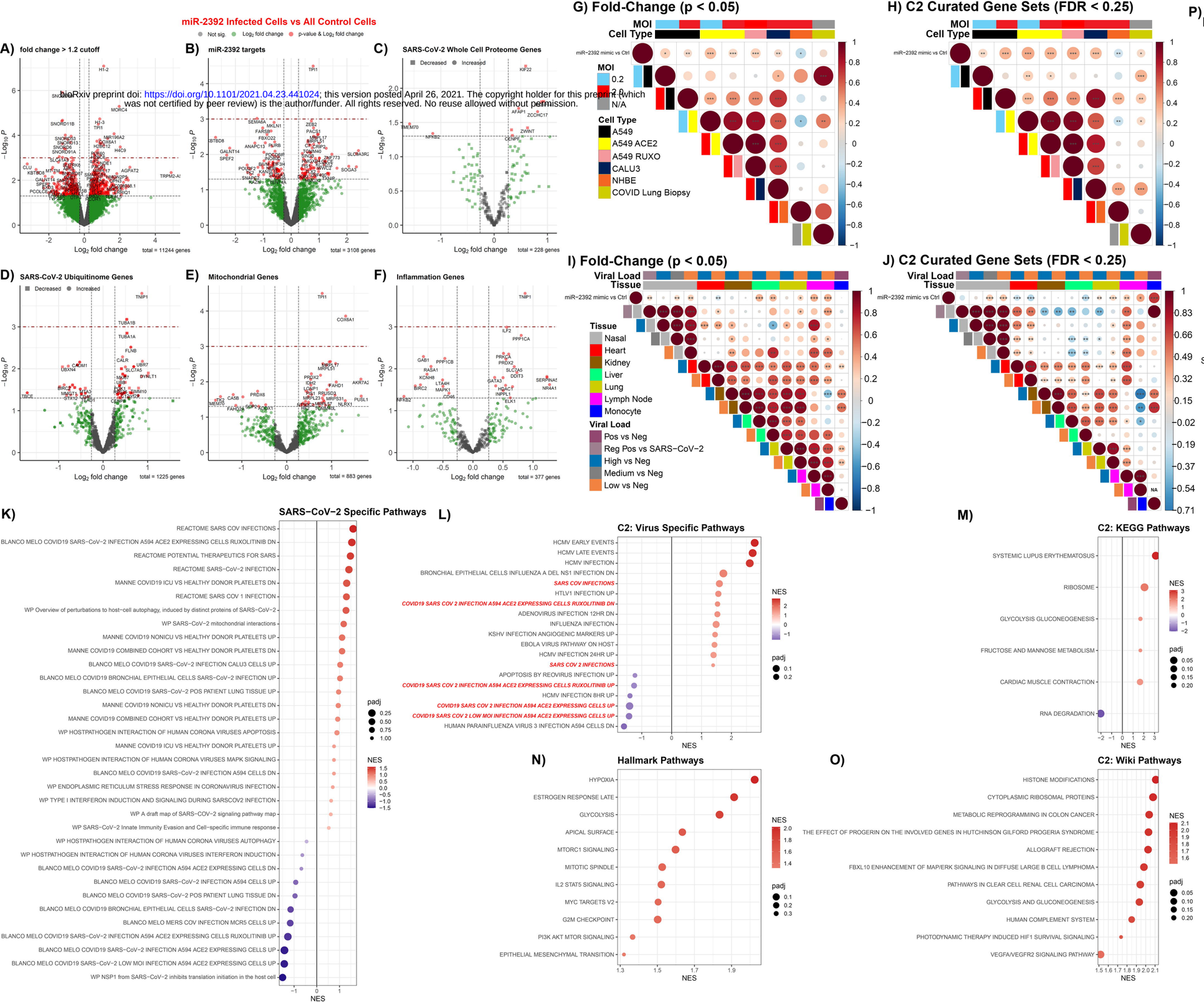

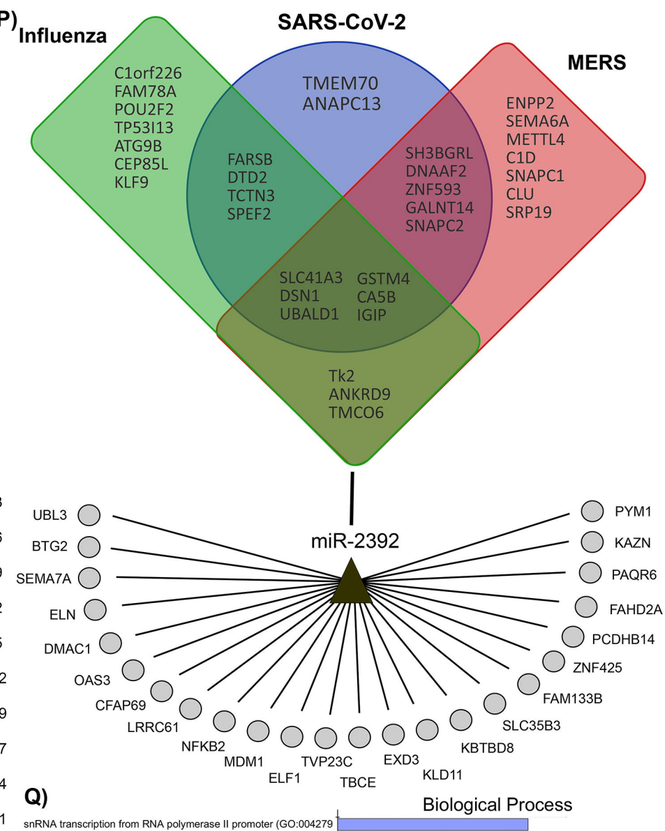

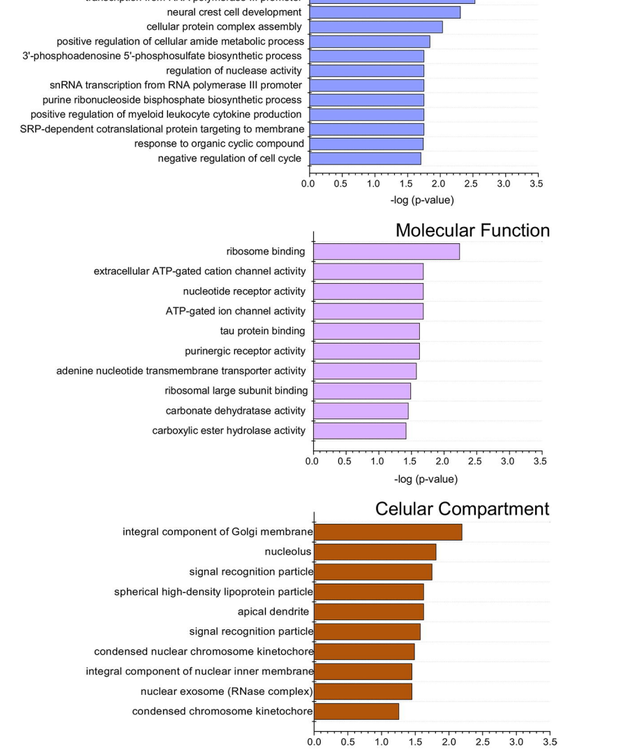

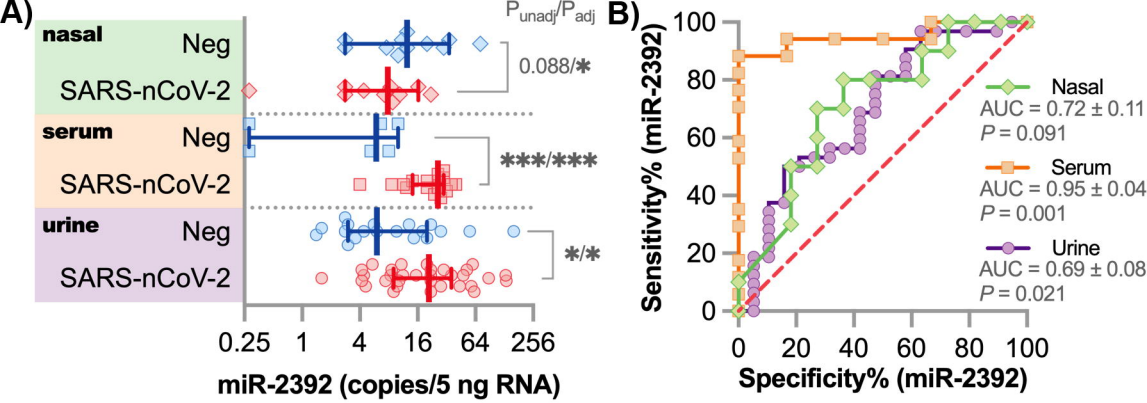

unadjusted = t-test on SARS (on log transformed values)
adjusted = mixed model corrected for age and sex (single terms)
*, **, *** = p < 0.05, 0.01, 0.001

AUC = area under the curve

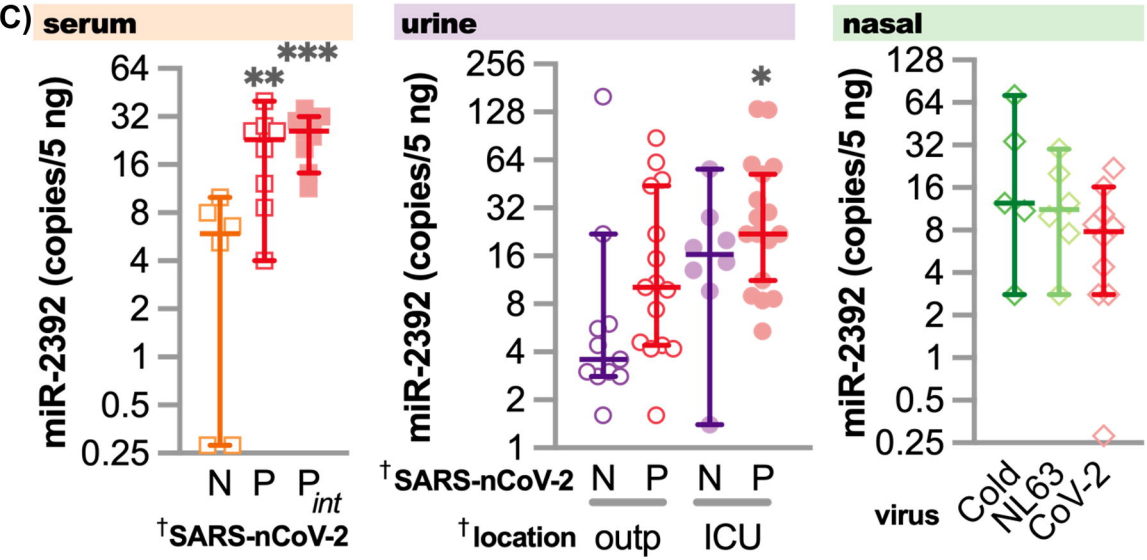

nasal and serum = ANOVA on log values
urine = 2-way ANOVA on log values
†, †† = p < 0.05, 0.01 from ANOVA
*,**,*** = p < 0.05, 0.01, 0.001 from Dunnet's post-test compared to Negative

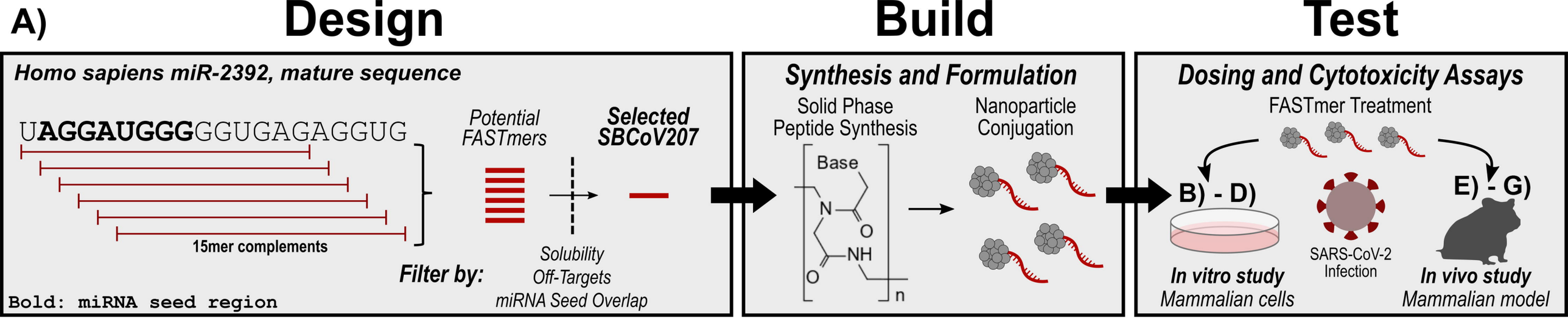

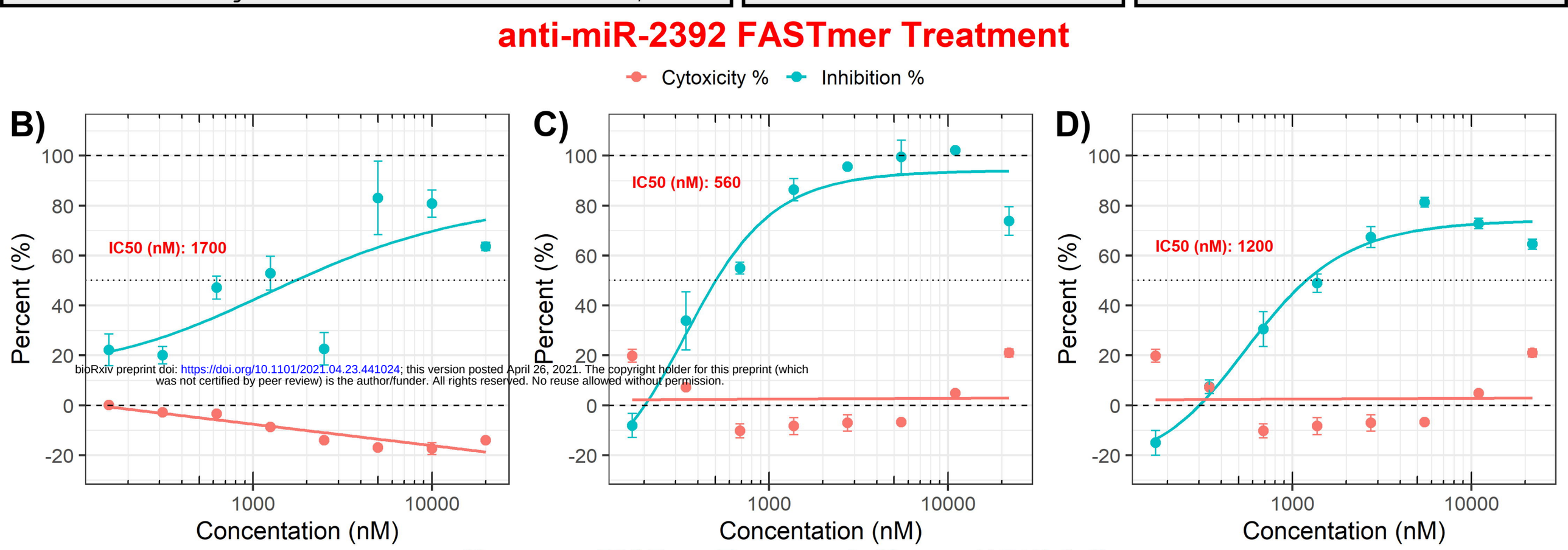

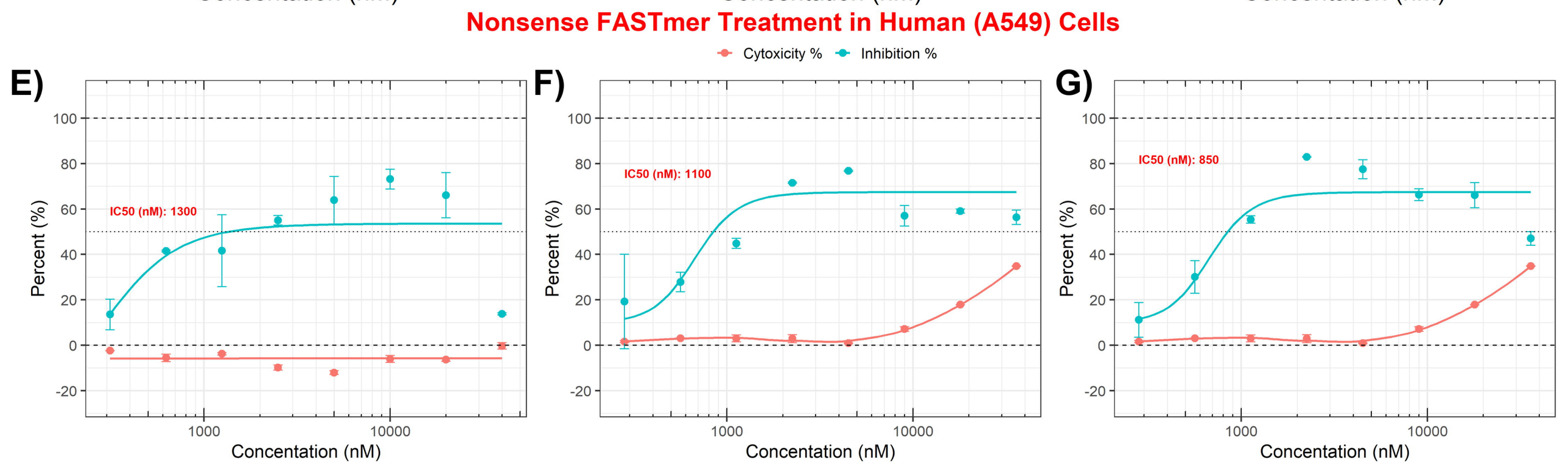

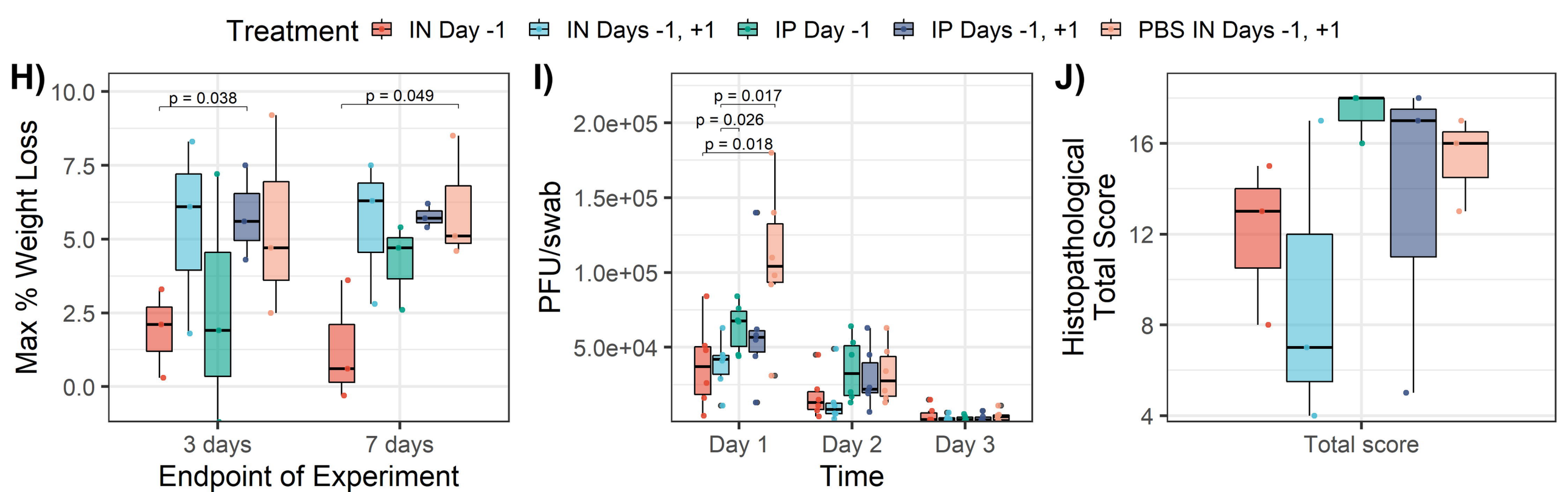

A) miR-2392 Predicted Diseases

Total # of Genes
50
100

Bilirubin
- Increased bilirubin level (finding)

Blood
- Increased serum lactate
- Serum creatinine raised
- Spherocytosis
- Anemia, hereditary spherocytic hemolytic
- Anemia
- SPHEROCYTOSIS, TYPE 1 (disorder)
- Serum iron raised
- Hyperproteinemia

Bone
- Hypoplastic pelvis
- Bone Marrow Diseases
- Abnormality of bone marrow cell morphology
- Hypoplastic sacrum
- Spinocerebellar ataxia 19
- Spinal Muscular Atrophy, Distal, Autosomal Recessive, 4
- Lobsteins Disease

Cancer
- Precancerous Conditions
- Malignant lymphoma, lymphocytic, intermediate differentiation, diffuse
- Intestinal Polyps
- Cellulitis
- Acute lymphocytic leukemia
- Fibrosarcoma
- Cecal Neoplasms
- Esophageal Neoplasms
- Von Hippel−Lindau Syndrome
- Benign neoplasm of central nervous system
- Mammary Neoplasms, Experimental

Cardiovascular
- Congestive heart failure
- Subaortic stenosis
- Aneurysm, Dissecting
- Microvesicular steatosis (disorder)
- Atrioventricular Septal Defect
- Heart failure
- Macrovesicular steatosis
- Orstavik Lindemann Solberg syndrome
- MICROVASCULAR COMPLICATIONS OF DIABETES, SUSCEPTIBILITY TO, 7 (finding)
- Heart defect, tongue hamartoma and polysyndactyly
- BRUGADA SYNDROME 9

CNS
- Encephalitis
- Stocco dos Santos syndrome
- Intermittent microsaccadic pursuits
- Cortical Congenital Hyperostosis
- Autism Spectrum Disorders
- Abnormality of the hypothalamus−pituitary axis

Deafness
- DEAFNESS, NONSYNDROMIC SENSORINEURAL, MITOCHONDRIAL
- DEAFNESS, AMINOGLYCOSIDE−INDUCED
- DEAFNESS, AUTOSOMAL RECESSIVE 74

Eye
- Coronary Aneurysm
- Gaze−evoked horizontal nystagmus

Female Reproductive System
- menstrual periods stopped for over 6 months
- Breech Presentation

Genomic Instability
- Genomic Instability
- HEMOCHROMATOSIS, TYPE 1

Gland
- Hyperparathyroidism

Hormone Deficiency
- Hypogonadotropic hypogonadism
- Hypogonadism, Isolated Hypogonadotropic
- Hypogammaglobulinemia

0.00 0.01 0.02 0.03 0.04
pvalue

Immune
- Increased IgM levels
- Cholangitis
- Hereditary spherocytosis
- Reduced natural killer cell activity
- X−Linked Lymphoproliferative Disorder
- Increased levels of IgG
- Decreased antibody level in blood
- Hemoglobin low
- Lymphoproliferative Syndrome, X−Linked, 2
- Abnormal glucose tolerance

Kidney
- Kidney Failure, Acute

Liver
- Liver enzymes abnormal
- Liver function tests abnormal finding
- Hepatic enzyme increased
- Hepatic Fibrosis, Congenital
- Increased hepatocellular lipid droplets
- Hepatitis C
- Fulminant hepatitis
- Hepatomegaly
- LIVER FAILURE, INFANTILE, TRANSIENT
- Liver Dysfunction

Male Infertility
- Azoospermia

Misc
- Lead Poisoning

Mitochondrial
- Cytochrome−c Oxidase Deficiency
- MITOCHONDRIAL MYOPATHY, INFANTILE, TRANSIENT
- Pentosuria

Muscle
- Hernia, Femoral

Oral
- Hamartoma of tongue
- Dentinogenesis Imperfecta
- CHARCOT−MARIE−TOOTH DISEASE, RECESSIVE INTERMEDIATE C

Respiratory
- Pleural effusion disorder

Short Stature
- Short femoral neck
- Short stature, severe disproportionate
- Short stature, disproportionate
- SHORT STATURE, ONYCHODYSPLASIA, FACIAL DYSMORPHISM, AND HYPOTRICHOSIS SYNDROME

Skin
- Icterus
- Porphyria, South African type
- Porphyria Cutanea Tarda, Type I
- Porphyria Cutanea Tarda

Smell
- Hyperesthesia

Sore Throat
- Lymphadenopathy
- pharyngitis recurrent

Spleen
- Splenomegaly

0.00 0.01 0.02 0.03 0.04
pvalue

B)

- N-ethyl-N-nitrosourea
- Arsenic trioxide
- Vorinostat (SAHA)
- Atorvastatin
- Trichostatin A (TSA)
- Curcumin
- Isoproterenol
- Formaldehyde
- Diethylstilbestrol
- Tert-butyl hydroperoxide (t-BHP)
- Ginsenoside Rh2
- 17beta-estradiol (E2)
- Nicotine
- Dexamethasone
- Reversine
- (S)-3,5-dihydroxyphenylglycine (DHPG)
- Hexahydro-1,3,5-trinitro-1,3,5-triazine (RDX)
- Perfluorooctane sulfonate
- Glucose
- 5-Fluorouracil

0 20 40 60
Predicted Score

C)

- CCT-018159
- opipramol
- JTE-013
- RG-7388
- metronidazole
- ubenimex
- calyculin
- pioglitazone
- floxuridine
- tamoxifen
- tioconazole
- palbociclib
- enzalutamide
- puromycin
- delanzomib
- FIT
- ZM-323881
- BMS-299897
- scoulerine
- PSI-7976

0 1 2
-normalised CMAP score